DFG-Schwerpunktprogramm 1324

„Extraktion quantifizierbarer Information aus komplexen Systemen"

Adaptive ADER Methods Using Kernel-Based Polyharmonic Spline WENO Reconstruction

T. Aboiyar, E. H. Georgoulis, A. Iske

Preprint 59

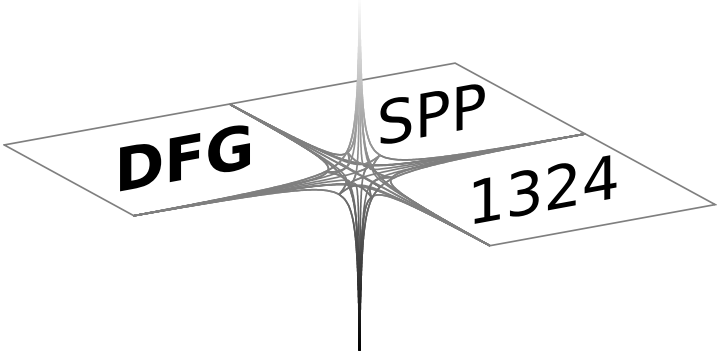

Edited by

AG Numerik/Optimierung
Fachbereich 12 - Mathematik und Informatik
Philipps-Universität Marburg
Hans-Meerwein-Str.
35032 Marburg

DFG-Schwerpunktprogramm 1324

„Extraktion quantifizierbarer Information aus komplexen Systemen"

Adaptive ADER Methods Using Kernel-Based Polyharmonic Spline WENO Reconstruction

T. Aboiyar, E. H. Georgoulis, A. Iske

Preprint 59

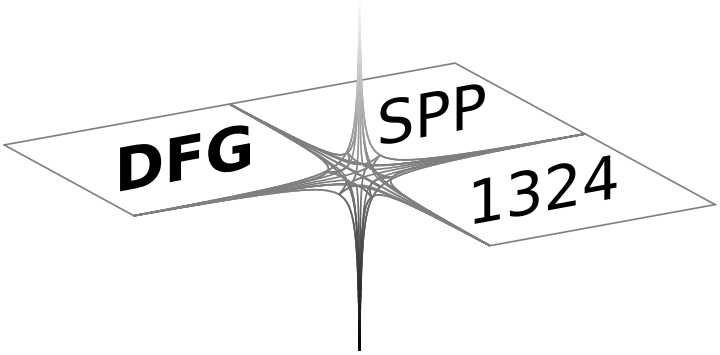

The consecutive numbering of the publications is determined by their chronological order.

The aim of this preprint series is to make new research rapidly available for scientific discussion. Therefore, the responsibility for the contents is solely due to the authors. The publications will be distributed by the authors.

ADAPTIVE ADER METHODS USING KERNEL-BASED POLYHARMONIC SPLINE WENO RECONSTRUCTION

TERHEMEN ABOIYAR*, EMMANUIL H. GEORGOULIS†, AND ARMIN ISKE‡

Abstract. An adaptive ADER finite volume method on unstructured meshes is proposed. The method combines high order polyharmonic spline WENO reconstruction with high order flux evaluation. Polyharmonic splines are utilised in the recovery step of the finite volume method yielding a WENO reconstruction that is stable, flexible and optimal in the associated Sobolev (Beppo-Levi) space. The flux evaluation is accomplished by solving generalised Riemann problems across cell interfaces. The mesh adaptation is performed through an a posteriori error indicator, which relies on the polyharmonic spline reconstruction scheme. The performance of the proposed method is illustrated by a series of numerical experiments, including linear advection, Burgers' equation, Smolarkiewicz's deformational flow test, and the five-spot problem.

Key words. finite volume methods, ADER flux evaluation, WENO reconstruction, hyperbolic conservation laws, polyharmonic splines.

AMS subject classifications. 65M12, 65M50, 65M60

1. Introduction.

During the last 30 years, *finite volume methods* (FVM) have gained great popularity as numerical schemes for hyperbolic problems. Classical FVM are typically of low order (cf. e.g., [15, 17]). High order FVM include *essentially non-oscillatory* (ENO) and the more sophisticated *weighted essentially non-oscillatory* (WENO) schemes (see, e.g., [1, 8, 10, 17, 24, 25, 38] and references therein) for the discretisation of the space variables. Available high order FVM often combine high order space discretisations with one-step or multistep time stepping methods, such as *total variation diminishing* Runge-Kutta (TVD-RK) methods. However, high order TVD-RK methods have a reduced region of absolute stability [9]. This essentially limits the order of TVD-RK time discretisations [20].

In the WENO framework, a collection of stencils is first selected in the neighbourhood of each cell (control volume). For each stencil, a high order recovery function is computed from the stencil's cell average values. The WENO reconstruction for the cell is then given by a weighted sum of the stencils' recovery functions. The weights are chosen so that unphysical oscillations in regions of low regularity of the solution (e.g. near sharp fronts and shocks) are avoided. In available (multivariate) WENO methods, local (multivariate) polynomial interpolation is used in the reconstruction step. Using multivariate polynomial interpolation in WENO reconstructions, however, has restrictions. Indeed, when using polynomial interpolation, the size of each stencil is required to match the dimension of the polynomial ansatz space; this reduces the flexibility in the stencil selection. This restriction is particularly severe for unstructured meshes, where for the sake of numerical stability enhanced flexibility in the stencil selection is of vital importance [1]. A standard remedy to circumvent this restriction is the use of least-squares approximation in the reconstruction step. Standard least-squares approximation, however, does usually *not* minimize the relevant quantities which are used for the definition of the WENO weights. This is regarded

*Department of Mathematics/Statistics/Computer Science, University of Agriculture, PMB 2373, Makurdi, Nigeria (t_aboiyar@yahoo.co.uk).

†Department of Mathematics, University of Leicester, University Road, Leicester, LE1 7RH, United Kingdom (Emmanuil.Georgoulis@mcs.le.ac.uk).

‡Department of Mathematics, University of Hamburg, Bundesstrasse 55, D-20146 Hamburg, Germany (iske@math.uni-hamburg.de).

as a major drawback of least-squares reconstructions, especially when it comes to approximate the solution in regions of low regularity.

Therefore, the development of stable high order FVM for hyperbolic problems is still an ongoing challenge.

Recently, ADER methods were introduced in [33, 34], and further developed in [29, 31, 36], to obtain finite volume schemes of arbitrary high order. In the concept of ADER, **A**rbitrary high order **DER**ivatives are used to construct high order flux evaluations, using generalised Godunov methods. The high order flux evaluation of the ADER method can be combined with high order finite volume space discretisations (e.g., WENO reconstructions), leading to an ADER-FVM of arbitrary high order. ADER schemes have very recently gained considerable popularity in a wide range of applications from engineering and physics, see e.g., [6, 21, 22, 23, 32].

The application of ADER schemes to nonlinear hyperbolic problems is a subject of active research. For the multi-dimensional case, ADER schemes on Cartesian grids can be found in [22, 23, 30]. ADER methods in combination with the discontinuous Galerkin method are introduced in [7]. *Adaptive* ADER methods on unstructured triangular meshes have recently been developed in [14], giving more flexible efficient high order ADER schemes. In [14], adaptive ADER methods are combined with high order polynomial WENO reconstructions.

Mesh adaptivity is particularly important for the computational efficiency of FVM. Indeed, the presence of lower dimensional locally singular behaviour of the solutions to hyperbolic problems (e.g., sharp gradients and discontinuities) require different resolutions in different regions of the computational domain. This can be accomplished using adaptive methods.

This work aims at the development of new stable adaptive FVM on unstructured meshes of arbitrary high order, both in space and in time, using the ADER methodology. More specifically, a novel framework for WENO reconstruction is proposed, whereby *kernel-based* interpolation (rather than polynomial interpolation) is utilised in the WENO reconstruction step. Kernel-based interpolation leads to ansatz spaces of variable dimensions, thereby can be applied to WENO reconstructions based on stencils of variable sizes, hence enhancing the flexibility of WENO reconstruction schemes. Our preferred choice of kernels are the family of the radial *polyharmonic splines*. Apart from the enhanced flexibility in the stencil selection, this particular choice has specific advantages concerning the numerical stability of local interpolation. Moreover, they are easily implemented in any space dimension. Furthermore, polyharmonic spline reconstruction leads to natural choices of *oscillation indicators*, as per required in the WENO reconstruction step. More specifically, the oscillation indicators are defined through the natural Sobolev semi-norms associated with the polyharmonic spline interpolation problem. For each stencil, the polyharmonic spline interpolant is the unique minimiser of the Sobolev semi-norm among all interpolants in the corresponding Sobolev space. Thus, the polyharmonic spline interpolant is – in that sense – the least oscillatory interpolant in the Sobolev space, which in turn improves the stability of the employed WENO reconstruction. This is supported by the numerical experiments presented in this work.

This work is organised as follows. In Section 2, the basic features of the finite volume method are discussed. In Section 3, we present the general framework of interpolation using polyharmonic splines. This includes a discussion on the numerical stability and other relevant properties of polyharmonic splines. Then, in Section 4, WENO reconstruction, based on polyharmonic splines, is introduced, before high or-

der flux evaluation by the ADER method is described in Section 5. Finally, Sections 6 and 7 contain a series of numerical experiments, illustrating the good performance of the proposed method, in terms of accuracy, efficiency and numerical stability.

2. The Finite Volume Method. We consider the scalar conservation law

$$u_t + \nabla \cdot F(u) = 0, \tag{2.1}$$

with $u \equiv u(t, \mathbf{x}) : I \times \Omega \to \mathbb{R}$, for an open bounded computational domain Ω and a time interval $I := (0, t_f]$, for some final time $t_f > 0$, with $F(u) := (f_1(u), \ldots, f_d(u))^T$ denoting the corresponding *flux function*. We equip (2.1) with the initial condition

$$u(0, \mathbf{x}) = u_0(\mathbf{x}), \quad \mathbf{x} \in \Omega, \tag{2.2}$$

along with (standard) suitable boundary conditions on the inflow part $\partial\Omega_-(t)$ of the boundary $\partial\Omega$, defined by

$$\partial\Omega_-(t) := \{\mathbf{x} \in \partial\Omega : F(u(t, \mathbf{x})) \cdot \mathbf{n}(\mathbf{x})) < 0\},$$

with $\mathbf{n}(\mathbf{x})$ denoting the outward unit normal vector to $\partial\Omega$ at the point $\mathbf{x} \in \partial\Omega$.

The construction of the finite volume method for the problem (2.1), (2.2) works as follows. The time interval I is first partitioned into sub-intervals $(t^n, t^{n+1}]$ of length $\tau^n := t^{n+1} - t^n$, for $n = 0, \ldots, N-1$, with $t^0 = 0$ and $t^N = t_f$. Moreover, for each $n = 0, 1, \ldots, N$, the computational domain Ω is partitioned into (possibly different) conforming shape-regular triangulations $\mathcal{T}^n = \{T\}_{T \in \mathcal{T}^n}$, consisting of d-dimensional closed simplices, i.e., triangles for $d = 2$ or tetrahedra for $d = 3$, which we shall refer to as *control volumes* or *cells*.

Integrating (2.1) over a space-time control volume $(t^n, t^{n+1}] \times T$, $T \in \mathcal{T}^n$, yields

$$\bar{u}_T(t^{n+1}) = \bar{u}_T(t^n) - \frac{1}{|T|} \sum_{j=1}^{d+1} \int_{t^n}^{t^{n+1}} \int_{\partial T_j} F(u) \cdot \mathbf{n}_j \, \mathrm{d}s \, \mathrm{d}t \qquad \text{for } n = 0, \ldots, N-1, \tag{2.3}$$

where

$$\bar{u}_T(t^n) := \frac{1}{|T|} \int_T u(t^n, \mathbf{x}) \mathrm{d}\mathbf{x} \qquad \text{for } n = 0, \ldots, N$$

is the *cell average* of the solution u on the control volume $T \in \mathcal{T}^n$ at time $t = t^n$. Moreover, ∂T_j, $j = 1, \ldots, d+1$, denote the faces of the simplex T and $\mathbf{n}_j$ is the outward unit normal vector to the face ∂T_j. Finally, $|T|$ and $|\partial T_j|$ are the d-dimensional volume of T and the $(d-1)$-dimensional volume of the face ∂T_j, respectively.

We approximate (2.3) by the (standard, one-step) *finite volume method*,

$$\bar{u}_T^{n+1} = \bar{u}_T^n - \frac{\tau^n}{|T|} \sum_{j=1}^{d+1} \tilde{F}_{T,j}^n, \qquad \text{for } n = 0, \ldots, N-1, \tag{2.4}$$

where $\bar{u}_T^n$ is an approximation to $\bar{u}_T(t^n)$ and the *numerical flux*

$$\tilde{F}_{T,j}^n \approx \frac{1}{\tau^n} \int_{t^n}^{t^{n+1}} \left(\int_{\partial T_j} F(u) \cdot \mathbf{n}_j \, \mathrm{d}s \right) \mathrm{d}t \tag{2.5}$$

is an approximation to the time-average flux across the face ∂T_j, $j = 1, \ldots, d+1$, of the control volume $T \in \mathcal{T}^n$ during the time interval $(t^n, t^{n+1}]$, $n = 0, \ldots, N-1$.

More specifically, upon discretisation of both the temporal and spatial integrals in (2.5), using a Gaussian quadrature with a number of q_t and q_x quadrature points in time and in space, respectively, the numerical flux $\tilde{F}^n_{T,j}$ is chosen as

$$\tilde{F}^n_{T,j} := \sum_{k=1}^{q_t} K_k |\partial T_j| \sum_{h=1}^{q_x} L_h F(u^{n,k,h}_{T,j}) \cdot \mathbf{n}_j, \tag{2.6}$$

where $u^{n,k,h}_{T,j}$ are approximations to the function values $u(t_{G_k}, \mathbf{x}_{G_h})$ (also known as *states* of the solution) at the Gaussian integration points $(t_{G_k}, \mathbf{x}_{G_h})$ with corresponding weights (K_k, L_h), for $1 \le k \le q_t$ and $1 \le h \le q_x$.

We remark that the (standard) finite volume method (2.4) is only a low order method. However, high order reconstruction techniques can be used to retrieve higher order approximations of the problem (2.1), (2.2) (see, e.g., [15, 17] and references therein). To avoid spurious oscillations near steep gradients and discontinuities, we shall employ WENO-type reconstructions relying on polyharmonic spline kernels for the interpolation step, rather than (standard) multivariate polynomials. The next section provides a brief discussion on kernel-based interpolation from cell average values using polyharmonic splines.

3. Interpolation of Cell Averages by using Polyharmonic Splines. Given a conforming triangulation $\mathcal{T} = \{T\}_{T\in\mathcal{T}}$ and a fixed cell $T \in \mathcal{T}$, we consider a *stencil*

$$\mathcal{S} := \{R\}_{R\in\mathcal{S}} \subset \mathcal{T},$$

of *size* $\#\mathcal{S} \in \mathbb{N}$, where we assume that T lies in $\mathcal{S}$, i.e., $T \in \mathcal{S}$. Note that any cell $R \in \mathcal{S}$ is associated with a linear functional λ_R, defined by

$$\lambda_R(u) = \frac{1}{|R|}\int_R u(\mathbf{x})\,\mathrm{d}\mathbf{x}, \qquad \text{for } R \in \mathcal{S} \text{ and } u(\mathbf{x}) \equiv u(t,\mathbf{x}),$$

i.e., λ_R is the cell average operator for R. We assume that the functionals $\{\lambda_R\}_{R\in\mathcal{S}}$ are linearly independent.

Now for the purpose of reconstructing given cell averages $\{\lambda_R(u)\}_{R\in\mathcal{S}}$ on stencil $\mathcal{S} \subset \mathcal{T}$, we consider using an *interpolant* of the form

$$s(\mathbf{x}) = \sum_{R\in\mathcal{S}} \alpha_R \lambda^{\mathbf{y}}_R \phi(\|\mathbf{x}-\mathbf{y}\|) + p(\mathbf{x}), \qquad p \in \mathcal{P}^d_m, \tag{3.1}$$

where $\phi(\|\cdot\|) : \mathbb{R}^d \to \mathbb{R}$ is a (fixed) *radial kernel function* w.r.t. the Euclidean norm $\|\cdot\|$ on $\mathbb{R}^d$ and $\lambda^{\mathbf{y}}_R$ denotes action of functional λ_R on variable $\mathbf{y}$, i.e.,

$$\lambda^{\mathbf{y}}_R \phi(\|\mathbf{x}-\mathbf{y}\|) = \frac{1}{|R|}\int_R \phi(\|\mathbf{x}-\mathbf{y}\|)\,\mathrm{d}\mathbf{y} \qquad \text{for } R \in \mathcal{S}.$$

Moreover, $\mathcal{P}^d_m$ denotes the space of all d-variate polynomials of order at most m (i.e., degree at most $m-1$), so that any polynomial $p \in \mathcal{P}^d_m$ can be represented as

$$p(\mathbf{x}) = \sum_{|\gamma|<m} \beta_\gamma \mathbf{x}^\gamma,$$

where $\gamma = (\gamma_1, \ldots, \gamma_d) \in \mathbb{N}^d_0$ is a multi-index of degree $|\gamma| := \gamma_1 + \ldots + \gamma_d$.

Now on given cell averages $\{\lambda_R(u)\}_{R\in\mathcal{S}}$, we consider solving the interpolation problem $u\big|_{\mathcal{S}} = s\big|_{\mathcal{S}}$, i.e.,

$$\lambda_R(u) = \lambda_R(s) \qquad \text{for all } R \in \mathcal{S}. \tag{3.2}$$

To this end, we need to determine $r+q$ parameters, where $q = \dim(\mathcal{P}^d_m) = \binom{m-1+d}{d}$ and $r = \#\mathcal{S}$. Noting that the linear conditions (3.2) amount to r equations, we consider solving (3.2) under linear constraints

$$\sum_{R\in\mathcal{S}} \alpha_R \lambda_R(p) = 0 \qquad \text{for all } p \in \mathcal{P}^d_m,$$

leading to the $(r+q)\times(r+q)$ linear equation system $\mathbf{A}\cdot\boldsymbol{\gamma} = \boldsymbol{\lambda}$ of the form

$$\begin{bmatrix} A & P \\ P^T & \mathbf{0} \end{bmatrix} \begin{bmatrix} \alpha \\ \beta \end{bmatrix} = \begin{bmatrix} \lambda \\ 0 \end{bmatrix} \tag{3.3}$$

with unknown vectors $\alpha = (\alpha_R)_{R\in\mathcal{S}} \in \mathbb{R}^r$ and $\beta = (\beta_\gamma)_{|\gamma|<m} \in \mathbb{R}^q$, matrices

$$A = (\lambda^{\mathbf{x}}_T \lambda^{\mathbf{y}}_R \phi(\|\mathbf{x}-\mathbf{y}\|))_{T,R\in\mathcal{S}} \in \mathbb{R}^{r\times r} \quad \text{and} \quad P = (\lambda_R(\mathbf{x}^\gamma))_{R\in\mathcal{S},|\gamma|<m} \in \mathbb{R}^{r\times q},$$

and right hand side $\lambda = (\lambda_R(u))_{R\in\mathcal{S}} \in \mathbb{R}^r$.

We finally remark that the linear system (3.3) has a solution, thus giving an interpolant s of the form (3.1), provided that the radial kernel ϕ is *conditionally positive definite* of order m on $\mathbb{R}^d$ (see [16] for details). Moreover, the solution will be unique, if the set $\{\lambda_R\}_{R\in\mathcal{S}}$ of cell average operators is $\mathcal{P}^d_m$-*unisolvent*, i.e., for $p \in \mathcal{P}^d_m$ the implication

$$\lambda_R(p) = 0 \quad \text{for all } R \in \mathcal{S} \qquad \Longrightarrow \quad p \equiv 0$$

holds, so that any polynomial $p \in \mathcal{P}^d_m$ can uniquely be reconstructed from its cell averages $\{\lambda_R(p)\}_{R\in\mathcal{S}}$. Finally, note that the interpolation scheme is invariant under translations and rotations.

3.1. Polyharmonic Spline Interpolation. We now make the specific choice $\phi \equiv \phi_{d,k} : [0,\infty) \to \mathbb{R}$ in (3.1), where

$$\phi_{d,k}(\|\cdot\|) = \begin{cases} \|\cdot\|^{2k-d} & \text{for } d \text{ odd;} \\ \|\cdot\|^{2k-d}\log(\|\cdot\|) & \text{for } d \text{ even,} \end{cases} \tag{3.4}$$

for $2k > d$. In this case, $m = k - \lceil d/2 \rceil + 1$ is the *order* of the conditionally positive definite kernel $\phi_{d,k}$. The so obtained class of radial kernels is known as *polyharmonic splines*.

We pair each polyharmonic spline $\phi_{d,k}$ with the Beppo-Levi space

$$\mathrm{BL}_k(\mathbb{R}^d) := \{v : D^\gamma v \in L^2(\mathbb{R}^d) \text{ for all } |\gamma| = k\} \subset C(\mathbb{R}^d),$$

equipped with the semi-norm $|\cdot|_{\mathrm{BL}_k(\mathbb{R}^d)}$, being defined by

$$|v|^2_{\mathrm{BL}_k(\mathbb{R}^d)} := \sum_{|\gamma|=k} \binom{k}{\gamma} \|D^\gamma v\|^2_{L^2(\mathbb{R}^d)}. \tag{3.5}$$

Due to Duchon [4], the resulting interpolant $s \in \mathrm{BL}_k(\mathbb{R}^d)$ in (3.1) satisfying (3.2) is the unique minimiser of the energy $|\cdot|_{\mathrm{BL}_k(\mathbb{R}^d)}$ among all interpolants $v \in \mathrm{BL}_k(\mathbb{R}^d)$ satisfying $v\big|_{\mathcal{S}} = u\big|_{\mathcal{S}}$, i.e., we have

$$|s|_{\mathrm{BL}_k(\mathbb{R}^d)} \leq |v|_{\mathrm{BL}_k(\mathbb{R}^d)} \qquad \text{for every } v \in \mathrm{BL}_k(\mathbb{R}^d) \text{ with } v\big|_{\mathcal{S}} = s\big|_{\mathcal{S}}. \tag{3.6}$$

This optimality of s gives rise to use the energy functional $|\cdot|_{\mathrm{BL}_k(\mathbb{R}^d)}$ as an oscillation indicator for the ensuing WENO reconstruction algorithm. In fact, since the energy value $|s|_{\mathrm{BL}_k(\mathbb{R}^d)}$ reflects the minimum of high order variations among all interpolants in $\mathrm{BL}_k(\mathbb{R}^d)$, the semi-norm $|\cdot|_{\mathrm{BL}_k(\mathbb{R}^d)}$ is a very suitable and most obvious choice for the WENO oscillation indicator, which – in contrast to previous WENO reconstruction schemes – comes naturally with the utilised interpolation scheme. Further details on this are explained in the following section.

A prominent example from the family of polyharmonic spline kernels is the *thin-plate spline* $\phi \equiv \phi_{2,2}(\|\cdot\|) = \|\cdot\|^2 \log(\|\cdot\|)$, which is a fundamental solution of the biharmonic equation on $\mathbb{R}^2$. For the thin-plate spline kernel, the interpolant s in (3.1) has the form

$$s(\mathbf{x}) = \sum_{R\in\mathcal{S}} \alpha_R \lambda_R^{\mathbf{y}} \left(\|\mathbf{x}-\mathbf{y}\|^2 \log(\|\mathbf{x}-\mathbf{y}\|)\right) + \beta_1 + \beta_2 x_1 + \beta_3 x_2,$$

where $\mathbf{x} = (x_1, x_2)^T \in \mathbb{R}^2$, and the corresponding Beppo-Levi semi-norm

$$|s|^2_{\mathrm{BL}_2(\mathbb{R}^2)} = \int_{\mathbb{R}^2} \left(s^2_{x_1x_1} + 2s^2_{x_1x_2} + s^2_{x_2x_2}\right) \mathrm{d}\mathbf{x}$$

gives the bending energy of a thin-plate of infinite extent.

Similarly, polyharmonic splines of higher order are defined by using the formulas (3.4) in (3.1). To make another relevant example, in our numerical results of Sections 6 and 7 concerning the two-dimensional case, $d = 2$, we work with the polyharmonic spline kernel $\phi_{2,3}(\|\cdot\|) = \|\cdot\|^4 \log(\|\cdot\|)$. In this case, the interpolant s in (3.1) has the form

$$s(\mathbf{x}) = \sum_{R\in\mathcal{S}} \alpha_R \lambda_R^{\mathbf{y}} \left(\|\mathbf{x}-\mathbf{y}\|^4 \log(\|\mathbf{x}-\mathbf{y}\|)\right) + \beta_1 + \beta_2 x_1 + \beta_3 x_2 + \beta_4 x_1^2 + \beta_5 x_1 x_2 + \beta_6 x_2^2.$$

The accuracy of Lagrangian interpolation by polyharmonic splines is analyzed in [11]. As proven in [11], $\phi_{d,k}$ has local approximation order $m = k - \lceil d/2 \rceil + 1$ for C^m functions. In other words, the local approximation order of polyharmonic spline interpolation, using $\phi_{d,k}$, is given by the order of their corresponding polynomial space $\mathcal{P}^d_m$ in (3.1). Since polynomials from $\mathcal{P}^d_m$ are exactly reconstructed, the expected accuracy order of polyharmonic spline interpolation is m. This complies with our numerical results in Section 6, where the thin-plate spline, $\phi_{2,2}$, yields second order spatial convergence, $m = 2$, while $\phi_{2,3}$ yields third order spatial convergence, $m = 3$.

3.2. Stable Evaluation of Polyharmonic Spline Interpolants. The numerical stability of interpolation by radial kernels is a critical issue in general, and so particularly for polyharmonic spline interpolation. This is due to a large spectral condition number of the collocation matrix $\mathbf{A}$ in (3.3), especially in situations, where the functionals $\{\lambda_R\}_{R\in\mathcal{S}}$ are *nearly* (i.e., numerically) linearly dependent. For further details concerning the conditioning of the system (3.3), we refer to the seminal work [18] of Narcowich and Ward.

As a remedy, a preconditioning strategy for Lagrange interpolation by polyharmonic splines is developed in [11]. The basic idea in [11] is to work with a locally scaled interpolation problem. In this section, we adapt the preconditioning method of [11] to the specific situation of this work.

In the present setting, the numerical stability of interpolation from cell average values is critical in situations, where the minimal Euclidean distance between barycentres of the distinct cells in a stencil $\mathcal{S} \subset \mathcal{T}$ is small. This is supported by our numerical observations. Moreover, this is consistent with the results in [18], where it is proven (for the case of Lagrange interpolation) that the spectral condition number of the interpolation matrix is bounded above by a monotonically decreasing function of the minimal Euclidean distance between the interpolation points.

As we shall see in Section 5, a stable implementation of the ADER method does not only require stable evaluations of the interpolants, but it also needs stable evaluations of their derivatives, necessitating the implementation of an efficient preconditioner. To this end, we extend the construction of the preconditioner in [11] (for Lagrange interpolation) to the present case of interpolation from cell averages.

We begin by considering the Lagrange representation of the interpolant s in (3.1), as given by

$$s(\mathbf{x}) = \sum_{R \in \mathcal{S}} \ell_R(\mathbf{x}) \lambda_R(u), \tag{3.7}$$

where the Lagrange basis functions ℓ_R are uniquely defined by the cardinal interpolation conditions

$$\lambda_R(\ell_T(\mathbf{x})) = \begin{cases} 1 & \text{for } T = R; \\ 0 & \text{for } T \neq R; \end{cases} \qquad \text{for } T, R \in \mathcal{S},$$

in combination with the moment conditions

$$\sum_{R \in \mathcal{S}} \ell_R(\mathbf{x}) \lambda_R(p) = p(\mathbf{x}) \qquad \text{for all } p \in \mathcal{P}_m^d,$$

requiring exact reconstruction of polynomials in $\mathcal{P}_m^d$.

The Lagrange basis functions $\zeta(\mathbf{x}) = (\ell_T(\mathbf{x}))_{R \in \mathcal{S}} \in \mathbb{R}^r$ can then be evaluated at any fixed argument $\mathbf{x} \in \mathbb{R}^d$ by the solution of the linear system

$$\begin{bmatrix} A & P \\ P^T & \mathbf{0} \end{bmatrix} \begin{bmatrix} \zeta(\mathbf{x}) \\ \eta(\mathbf{x}) \end{bmatrix} = \begin{bmatrix} \theta(\mathbf{x}) \\ \kappa(\mathbf{x}) \end{bmatrix}, \tag{3.8}$$

or, $\mathbf{A} \cdot \boldsymbol{\mu}(\mathbf{x}) = \boldsymbol{\nu}(\mathbf{x})$, in short-hand notation, where

$$\begin{aligned} \eta(\mathbf{x}) &= (\eta_\gamma(\mathbf{x}))_{|\gamma|<m} \in \mathbb{R}^q, \\ \theta(\mathbf{x}) &= (\lambda_R^{\mathbf{y}} \phi(\|\mathbf{x} - \mathbf{y}\|))_{R \in \mathcal{S}} \in \mathbb{R}^r, \\ \kappa(\mathbf{x}) &= (\mathbf{x}^\gamma)_{|\gamma|<m} \in \mathbb{R}^q. \end{aligned}$$

The Lagrange representation (3.7) of the interpolant s is particularly useful when analysing the effect of local affine transformations. To see this, we consider for a fixed stencil $\mathcal{S}$ and fixed cell $T \in \mathcal{S}$ the affine map $F_T : \mathbb{R}^d \to \mathbb{R}^d$, defined by

$$F_T(\mathbf{x}) = (\mathbf{x} - \mathbf{b}_T)/h_T,$$

where $\mathbf{b}_T$ and h_T denote the barycentre and the diameter of T, respectively. We perform the change of variables $\hat{\mathbf{x}} = F_T(\mathbf{x})$ and consider the corresponding transformed interpolation problem $u\big|_{\hat{\mathcal{S}}} = s\big|_{\hat{\mathcal{S}}}$, i.e.,

$$\lambda_{\hat{R}}(u) = \lambda_{\hat{R}}(s), \qquad \text{for all } \hat{R} \in \hat{\mathcal{S}}, \tag{3.9}$$

on the *pulled-back stencil* $\hat{\mathcal{S}} := \{\hat{R}\}_{\hat{R}\in\hat{\mathcal{S}}}$, where $\hat{R} := F_T(R)$ for $R \in \mathcal{S}$.

This leads us to the linear system, corresponding to (3.8),

$$\begin{bmatrix} \hat{A} & \hat{P} \\ \hat{P}^T & \mathbf{0} \end{bmatrix} \begin{bmatrix} \hat{\zeta}(\hat{\mathbf{x}}) \\ \hat{\eta}(\hat{\mathbf{x}}) \end{bmatrix} = \begin{bmatrix} \hat{\theta}(\hat{\mathbf{x}}) \\ \hat{\kappa}(\hat{\mathbf{x}}) \end{bmatrix},$$

or, $\hat{\mathbf{A}} \cdot \hat{\boldsymbol{\mu}}(\hat{\mathbf{x}}) = \hat{\boldsymbol{\nu}}(\hat{\mathbf{x}})$, in short hand notation, where

$$\begin{aligned}
\hat{\zeta}(\hat{\mathbf{x}}) &= \left(\hat{\ell}_{\hat{R}}(\hat{\mathbf{x}})\right)_{\hat{R}\in\hat{\mathcal{S}}} \in \mathbb{R}^r, \\
\hat{\eta}(\hat{\mathbf{x}}) &= (\hat{\eta}_\gamma(\hat{\mathbf{x}}))_{|\gamma|<m} \in \mathbb{R}^q, \\
\hat{\theta}(\hat{\mathbf{x}}) &= \left(\lambda^{\hat{\mathbf{y}}}_{\hat{R}}\phi(\|\hat{\mathbf{x}} - \hat{\mathbf{y}}\|)\right)_{\hat{R}\in\hat{\mathcal{S}}} \in \mathbb{R}^r, \\
\hat{\kappa}(\hat{\mathbf{x}}) &= (\hat{\mathbf{x}}^\gamma)_{|\gamma|<m} \in \mathbb{R}^q,
\end{aligned}$$

and

$$\hat{A} = \left(\lambda^{\mathbf{x}}_{\hat{T}}\lambda^{\mathbf{y}}_{\hat{R}}\phi(\|\mathbf{x}-\mathbf{y}\|)\right)_{\hat{T},\hat{R}\in\hat{\mathcal{S}}} \in \mathbb{R}^{r\times r} \quad \text{and} \quad \hat{P} = \left(\lambda_{\hat{R}}(\mathbf{x}^\gamma)\right)_{\hat{R}\in\hat{\mathcal{S}},|\gamma|<m} \in \mathbb{R}^{r\times q}.$$

Note that the Lagrange basis $\hat{\zeta}(\hat{\mathbf{x}})$ immediately yields the solution s of the transformed interpolation problem (3.9) by

$$s(\hat{\mathbf{x}}) = \sum_{\hat{R}\in\hat{\mathcal{S}}} \hat{\ell}_{\hat{R}}(\hat{\mathbf{x}}) \cdot \lambda_{\hat{R}}(u).$$

Moreover, note that any derivative $D^\gamma\zeta(\mathbf{x})$, $|\gamma| < m$, of the Lagrange basis functions $\zeta(\mathbf{x})$ can be expressed as

$$D^\gamma\zeta(\mathbf{x}) = h_T^{-|\gamma|} D^\gamma\hat{\zeta}(\hat{\mathbf{x}}) \qquad \text{for every } \mathbf{x} \in \mathbb{R}^d. \tag{3.10}$$

Using (3.10) we are now in a position to propose a numerically stable evaluation of $D^\gamma s$ for $|\gamma| < m$. This is done by rewriting $D^\gamma s(\mathbf{x})$ as

$$\begin{aligned}
D^\gamma s(\mathbf{x}) &= \langle D^\gamma\zeta(\mathbf{x}), \lambda\rangle = \langle h_T^{-|\gamma|} D^\gamma\hat{\zeta}(\hat{\mathbf{x}}), \lambda\rangle = h_T^{-|\gamma|}\langle D^\gamma\hat{\boldsymbol{\mu}}(\hat{\mathbf{x}}), \boldsymbol{\lambda}\rangle \\
&= h_T^{-|\gamma|}\langle \hat{\mathbf{A}}^{-1} D^\gamma\hat{\boldsymbol{\nu}}(\hat{\mathbf{x}}), \boldsymbol{\lambda}\rangle = h_T^{-|\gamma|}\langle D^\gamma\hat{\boldsymbol{\nu}}(\hat{\mathbf{x}}), \hat{\mathbf{A}}^{-1}\boldsymbol{\lambda}\rangle,
\end{aligned}$$

where $\langle\cdot,\cdot\rangle$ denotes the Euclidean inner product, and $\boldsymbol{\lambda}$ is the right hand side in (3.3). Due to the conformity and the shape-regularity assumptions on the simplicial mesh $\mathcal{T}$, $\mathcal{T}$ is locally quasi-uniform, i.e., the sizes and shapes of neighbouring simplices in a stencil $\mathcal{S} \subset \mathcal{T}$ are not subject to strong variations. In this case, the matrix $\hat{\mathbf{A}}$ has a *small* spectral condition number, and so the evaluation of the derivative

$$D^\gamma s(\mathbf{x}) = h_T^{-|\gamma|}\langle D^\gamma\hat{\boldsymbol{\nu}}(\hat{\mathbf{x}}), \mathbf{b}\rangle$$

is numerically stable by solving the preconditioned system $\hat{\mathbf{A}}\mathbf{b} = \boldsymbol{\lambda}$ rather than solving the unpreconditioned system $\mathbf{A}\boldsymbol{\gamma} = \boldsymbol{\lambda}$ in (3.3).

4. Kernel-Based WENO Reconstruction. We shall now apply polyharmonic spline interpolation to weighted essentially non-oscillatory (WENO) methods for the reconstruction step of finite volume methods, and so obtain kernel-based WENO reconstruction methods.

4.1. Oscillation Indicator and Weights. For each cell $T \in \mathcal{T}$, we consider a finite number of pairwise distinct stencils $\mathcal{S}_i \subset \mathcal{T}$ with $T \in \mathcal{S}_i$, each giving a unique polyharmonic spline interpolant s_i, which can be computed from the available cell averages in (2.4). We then define the WENO reconstruction s as a convex combination

$$s := \sum_i \omega_i s_i \qquad \text{with} \qquad \sum_i \omega_i = 1 \tag{4.1}$$

of the interpolants s_i with non-negative weights ω_i. We remark that the choice of the weights ω_i is crucial in order to damp down spurious oscillations in the numerical solution. In fact, ω_i should be small whenever s_i is highly oscillatory (indicating a large gradient/discontinuity of the solution across the region of the stencil $\mathcal{S}_i$); on the contrary, ω_i should be large whenever s_i varies slowly in the region of the stencil $\mathcal{S}_i$ (indicating a region of local smoothness).

As already explained in the previous section, the Beppo-Levi semi-norm $|\cdot|_{\mathrm{BL}_k(\mathbb{R}^d)}$ in (3.5) is a suitable oscillation measure for elements from the Beppo-Levi space $\mathrm{BL}_k(\mathbb{R}^d)$. Moreover, due to the optimality of polyharmonic spline interpolation in (3.6), it is most natural to define the *oscillation indicator* $\mathcal{I} : \mathrm{BL}_k(\mathbb{R}^d) \to [0, \infty)$ by

$$\mathcal{I}(v) := |v|^2_{\mathrm{BL}_k(\mathbb{R}^d)} \qquad \text{for } v \in \mathrm{BL}_k(\mathbb{R}^d).$$

For fixed parameters $\epsilon > 0$ and $\rho \in \mathbb{N}$, let

$$\tilde{\omega}_i := (\epsilon + \mathcal{I}(s_i))^{-\rho}, \tag{4.2}$$

and define the non-negative weights ω_i in (4.1) by

$$\omega_i := \frac{\tilde{\omega}_i}{\sum_j \tilde{\omega}_j},$$

so that $\sum_i \omega_i = 1$.

The parameter ϵ in (4.2) is a small positive number used to avoid division by zero. We remark that the numerical results are usually not sensitive to the choice of ϵ. In general, large values ϵ are admissible for smooth regions of the solution, but may lead to small (undesired) oscillations near shocks. Therefore, smaller values ϵ are preferably used for problems with discontinuous/rapidly varying solutions. In our numerical examples, we let $\epsilon = 10^{-6}$ (cf. [10, 14]).

The positive integer ρ in (4.2) serves to control the sensitivity of the weights with respect to the oscillation $\mathcal{I}$. Note that in the limit, when ρ tends to infinity, the resulting WENO scheme becomes a classical ENO scheme. In contrast, when ρ tends to zero, this leads to a WENO scheme with equal weights ω_i, which may become oscillatory or even unstable. In our implementation we let $\rho = 2$, which turns out to be large enough to effectively reduce undesired oscillations near discontinuities, but small enough to improve upon the classical ENO scheme.

4.2. Stencil Selection. Now we discuss the selection of the stencils $\mathcal{S}_i$. As documented in previous work [8, 14, 27] on polynomial-based WENO reconstruction,

the selection of stencils is a critical and challenging task which influences heavily the approximation behaviour of the resulting WENO reconstruction.

In the case of polynomial WENO reconstruction schemes, the number of cells $\#\mathcal{S}_i$ in each stencil $\mathcal{S}_i$ is required to match the dimension of the polynomial space (cf., e.g., [14] and the references therein). This severe restriction, however, diminishes the desired flexibility in the stencil selection, which is particularly critical in regions where the solution is rapidly varying or even discontinuous. A well-known remedy to circumvent this restriction is the use of least-squares approximation instead of interpolation, especially in situations where the condition number of the interpolation matrix is very large, or, when the number of degrees of freedom in a stencil does not match the dimension of the polynomial space. Standard least-squares approximation, however, does usually *not* minimize the relevant quantities which are used for the definition of the WENO weights. In fact, least-squares approximation does rather lead to *smooth* reconstructions, whose corresponding smoothness functional does usually not match the energy functional of the WENO oscillation indicator.

In contrast, the WENO reconstruction using polyharmonic splines described above requires that for any stencil $\mathcal{S}_i$ its size $r = \#\mathcal{S}_i$ exceeds the dimension q of the polynomial space, i.e., $r \geq q$, while simultaneously minimizing the physically relevant Beppo-Levi norm. For instance, in two dimensions, thin-plate spline WENO reconstruction merely requires that each stencil contains at least three triangles. This additional flexibility gives polyharmonic spline WENO reconstructions a clear advantage over polynomial WENO reconstruction schemes when applied to complex or unstructured grids, without excessive smearing of any sharp gradients/discontinuities present in the PDE solution.

Nevertheless, given the additional flexibility in the stencil design, the construction of suitable stencils requires particular care. Motivated by previous work [8, 14, 27], three different types of stencils are constructed: isotropic *centred stencils*, anisotropic *forward sector stencils* and *backward sector stencils*. We describe the construction of the three different types of stencils, restricting the discussion to the two-dimensional setting, for the sake of simplicity. The generalisation of these constructions to three (and higher) dimensions is rather intuitive: we refer to the algorithm of Dumbser and Käser [5] for further details.

For a cell $T \in \mathcal{S}$, the centred stencils are constructed by recursively including levels of *von Neumann neighbours* to T. The level-0 von Neumann neighbours are defined to be the cells sharing a common edge with T. The level-1 von Neumann neighbours are, in turn, the cells sharing a common edge with level-0 von Neumann neighbours of T, and so forth (see, e.g., [14] for a formal definition). Figure 4.1 shows three different examples of cell centred stencils around one triangular cell $T \in \mathcal{S}$ (red), with each stencil comprising seven triangles (one red, six green) lying in the level-1 von Neumann neighbourhood of T.

The construction of forward sector stencils is described as follows. A forward sector of a cell T is a sector spanned by two different edges of T that contains T itself (see Figure 4.2 for an illustration). Therefore, any triangular cell T has three different forward sectors. Now, for each forward sector of T, a corresponding forward sector stencil may only contain a finite (but arbitrary) number of cells whose barycentres lie in that forward sector. Figure 4.2 shows three different examples for forward sector stencils of one triangle $T \in \mathcal{S}$ (red), each comprising seven triangles (one red, six green).

Finally, the backward sectors of a cell T are defined using the midpoints of the

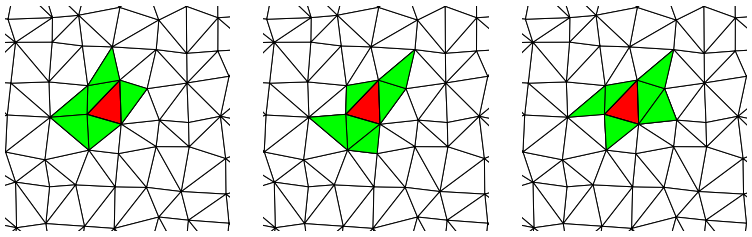

FIG. 4.1. *Three cell centred stencils of size seven around triangle T (red).*

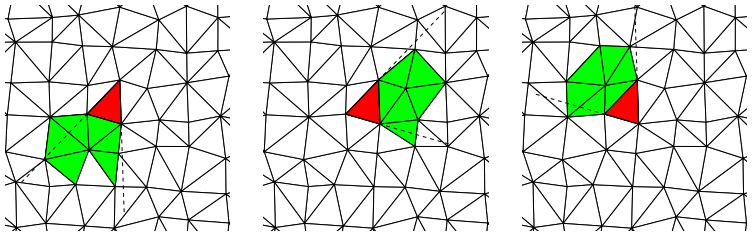

FIG. 4.2. *Three forward stencils of size seven generated by triangle T (red). The three corresponding forward sectors are marked by dashed lines, respectively.*

edges in T: the backward sector corresponding to each midpoint m_e of an edge e of T is the sector with origin m_e and spanned by the lines passing through the midpoints of the other two edges in T lying opposite to e (see Figure 4.3 for an illustration). The corresponding backward sector stencil may contain a finite (but arbitrary) number of triangles whose barycentres lie in that backward sector. Figure 4.3 shows three different examples for backward sector stencils of one triangle $T \in \mathcal{S}$ (red), each comprising seven triangles (one red, six green).

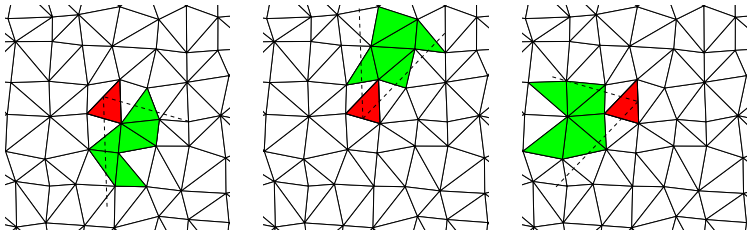

FIG. 4.3. *Three backward stencils of size seven generated by triangle T (red). The three corresponding backward sectors are marked by dashed lines, respectively.*

After extensive numerical tests in two dimensions, we observed that seven stencils (one centred, three forward sector, and three backward sector stencils) of size four are sufficient for WENO reconstructions using thin-plate splines, $\phi_{2,2}(\|\cdot\|) = \|\cdot\|^2 \log(\|\cdot\|)$, when the problem admits smooth solutions. On the other hand, for problems with locally discontinuous or rapidly varying solutions, seven stencils of size seven appear to provide the required flexibility to reduce numerical oscillations. For reconstructions using $\phi_{2,3}(\|\cdot\|) = \|\cdot\|^4 \log(\|\cdot\|)$ it was observed that using nine stencils (three centred, three forward sector, and three backward sector stencils) of size nine gave a stable reconstruction in all cases.

In contrast to this, in our previous work [14] on ADER schemes using polynomial

WENO reconstructions, we rely, for each triangle T, on nine stencils (three centred, three forward, three backward), where the number of triangles in each stencil is fixed by the dimension of the polynomial space.

On the basis of our numerical observations, we remark that it is possible to use a variable stencil size in various parts of the computational domain: one can use stencils of smaller size in smooth regions of the solution and larger size stencils in non-smooth ones, resulting to substantial savings in practical computations. We refer to [2] for a detailed discussion on adaptive stencil selection.

5. High Order Flux Evaluation by using the ADER Method. In this section, we give a brief account of the ADER method for flux evaluation of arbitrary high order [29, 34, 35, 37].

5.1. Flux Evaluation. To evaluate the numerical flux (2.6), we have to compute the approximations $u_{T,j}^{n,k,h}$ to the function values $u(t_{G_k}, \mathbf{x}_{G_h})$.

In the ADER method, the term $u(t_{G_k}, \mathbf{x}_{G_h})$ is approximated via a truncated Taylor series expansion w.r.t. the time variable. In this setting, a local (orthogonal) coordinate system $(\tau, x_{\mathbf{n}})$ is used, where τ is the local time $\tau := t - t^n$ with $t \in [t^n, t^{n+1}]$ and $x_{\mathbf{n}} := \mathbf{x} - \mathbf{x}_{G_h}$, i.e., $x_{\mathbf{n}}$ is a local coordinate oriented along the outer normal vector, with origin $\mathbf{x}_{G_h}$. Then, the *interface state* $u(\tau, 0)$ (i.e., the state at $\mathbf{x} = \mathbf{x}_{G_h}$) is approximated via the Taylor series expansion

$$u(\tau, 0) \approx u_m(\tau, 0) := u(0, 0) + \sum_{j=1}^{m-1} \frac{\tau^j}{j!} \partial_t^{(j)} u(0, 0), \tag{5.1}$$

where m is the *local approximation order* of the polyharmonic spline interpolation scheme used in the WENO reconstruction [11]. According to the ADER method, the Taylor expansion (5.1) is used to evaluate u_m at any intermediate time $t_{G_k} \in [t^n, t^{n+1}]$, giving an m-th order approximation to $u(t_{G_k}, 0)$.

The evaluation of the time derivatives of u on the right hand side of (5.1) is the subject of discussion in the following two subsections.

The leading term. The leading term $u^* := u(0, 0)$ in the expansion (5.1), commonly known as the *Godunov state* of u, represents the first-instant interaction of the initial data via the PDE (2.1). The Godunov state u^* is, according to the classical Godunov method, computed by solving a *generalised Riemann problem* (GRP) at the cell interface.

Now at each Gaussian point $\mathbf{x}_{G_h}$ on a cell interface, the original PDE problem can be approximated by a series of one-dimensional GRPs oriented towards the normal direction of the cell interface [37]. More specifically, let $\partial_{\mathbf{n}}$ denote the derivative in the direction normal to the interface (i.e., the direction of $x_{\mathbf{n}}$), let s_L denote the WENO reconstruction (on the actual cell T), and let s_R be the corresponding WENO reconstruction of the adjacent cell (with common interface to T). Then, the one-dimensional GRP is defined by the PDE

$$v_t + \partial_{\mathbf{n}} F(v) = 0$$

with initial conditions

$$v(0, x_{\mathbf{n}}) = \begin{cases} u_L := \lim_{\mathbf{x} \to \mathbf{x}_{G_h}^-} s_L(\mathbf{x}) & \text{for } x_{\mathbf{n}} < 0, \\ u_R := \lim_{\mathbf{x} \to \mathbf{x}_{G_h}^+} s_R(\mathbf{x}) & \text{for } x_{\mathbf{n}} > 0. \end{cases}$$

We refer to u_L and u_R as *left* and *right* states, respectively.

The higher order derivatives. To compute the high order time derivatives $\partial_t^{(j)} u(t, \mathbf{x})$, $j = 1, \ldots, m-1$, at the local interface $(0, 0)$, we shall employ the classical *Cauchy-Kowaleskaja procedure* (also known as *Lax-Wendroff procedure*), whereby we replace the time derivatives with spatial derivatives. This is done by using the governing PDE (2.1).

To be more precise, the Cauchy-Kowaleskaja procedure is formulated as follows: the PDE (2.1) can be rewritten as

$$u_t = -\sum_{i=1}^{d} f_i'(u) u_{x_i}, \tag{5.2}$$

where $f_i'(u) = \frac{\partial f_i(u)}{\partial u}$, $i = 1, \ldots, d$, thereby expressing u_t by first order space derivatives. Now the second order time derivative u_{tt} can be computed via

$$u_{tt} = -\sum_{i=1}^{d} \left(f_i^{''}(u) u_t u_{x_i} + f_i'(u) u_{t x_i} \right),$$

where the mixed derivatives $u_{t x_i}$, $i = 1, \ldots, d$, are obtained by differentiating (5.2) with respect to x_i,

$$u_{t x_j} = -\sum_{i=1}^{d} \left(f_i^{''}(u) u_{x_i} u_{x_j} + f_i'(u) u_{x_i x_j} \right), \qquad \text{for } j = 1, \ldots, d,$$

and so on for the higher order derivatives [29, 35].

Therefore, the problem of computing the time derivatives of u in (5.1) can be reduced to the problem of computing the unknown spatial derivatives at the quadrature points on the cell interfaces. To this end, following [29, 35], we first linearise the PDE (2.1) about the Godunov state u^*, before we differentiate the linearised PDE to arrive at

$$\varphi_t^{\gamma} + \nabla \cdot F^*(\varphi^{\gamma}) = 0,$$

with $F^*(v) = (f_1'(u^*)v, \ldots, f_d'(u^*)v)^T$ and $\varphi^{\gamma} := D^{\gamma} \tilde{u}$, for multi-indices γ, $|\gamma| < m$, where $\tilde{u}$ is the solution to the *linearised* problem

$$\tilde{u}_t + \nabla \cdot F^*(\tilde{u}) = 0.$$

The computation of φ^{γ} at $\mathbf{x}_{G_h}$ is performed via the solution of the (standard) Riemann problem [37]

$$\varphi_t^{\gamma} + \partial_{\mathbf{n}} F^*(\varphi^{\gamma}) = 0$$

with initial conditions

$$\varphi^{\gamma}(0, x_{\mathbf{n}}) = \begin{cases} \lim_{\mathbf{x} \to \mathbf{x}_{G_h}^-} D^{\gamma} s_L(\mathbf{x}) & \text{for } x_{\mathbf{n}} < 0, \\ \lim_{\mathbf{x} \to \mathbf{x}_{G_h}^+} D^{\gamma} s_R(\mathbf{x}) & \text{for } x_{\mathbf{n}} > 0. \end{cases}$$

The so computed Godunov state u^* and the corresponding higher order values φ^{γ}, $|\gamma| < m$, are, in combination with the Cauchy-Kowaleskaja procedure, used to obtain the desired approximations to the time derivatives $\partial_t^{(j)} u(0, 0)$ for $0 \leq j \leq m-1$.

These in turn, when inserted into the Taylor series expansion (5.1), yield m-th order approximations $u_{T,j}^{n,k,h}$ of the function values $u(t_{G_k}, \mathbf{x}_{G_h})$.

In summary, high order flux evaluation using the ADER method requires the solution of one (possibly nonlinear) generalised Riemann problem (GRP) and a sequence of $m-1$ linear (standard) Riemann problems for the space derivatives. This renders the ADER method as a high order generalisation of the classical Godunov method. For further details concerning the ADER method, we refer to the seminal papers [29, 34, 37] and references therein.

5.2. The CFL Condition. To maintain the stability of the ADER method, we follow our previous work [14], where the time step size τ^n is restricted by the *CFL condition*,

$$\tau^n \leq \min_{T\in\mathcal{T}^n} \frac{\rho_T}{\eta_T^{\max}},$$

where ρ_T is the radius of the inscribed $(d-1)$-dimensional sphere of a cell $T \in \mathcal{T}^n$ and

$$\eta_T^{\max} := \max |F'(u)\cdot \mathbf{n}| \qquad \text{with } F'(u) := (f_1'(u), \ldots, f_d'(u))^T$$

denotes the maximum normal characteristic speed of the flux, where the maximum is taken over all Gaussian integration points of the cell interfaces of T (see [14] for further details).

6. Numerical Results on Quasi-Uniform Triangular Meshes. We have implemented the proposed ADER method in two space dimensions (i.e., $d = 2$) to evaluate its performance in practice. For the WENO reconstruction step, we work with two different polyharmonic spline kernels in (3.4): (a) thin-plate splines $\phi_{2,2}$ of order $m = 2$; (b) $\phi_{2,3}$ of order $m = 3$. As this work aims primarily in providing a proof-of-concept for the use and performance of non-polynomial reconstructions, we confine ourselves (for brevity and simplicity) to a rather extensive account of numerical experiments using second and third order polyharmonic spline kernels. We stress, however, that it is by all means possible to consider higher order space WENO reconstructions in conjunction within higher order ADER methods.

6.1. Linear Advection. We consider solving the linear advection equation

$$u_t + u_{x_1} + u_{x_2} = 0 \qquad \text{where } \mathbf{x} = (x_1, x_2)$$

for $u \equiv u(t, \mathbf{x}) : [0,1] \times [-0.5, 0.5]^2 \to \mathbb{R}$ with the initial condition

$$u_0(\mathbf{x}) = u(0,\mathbf{x}) = \sin^2\left(\pi\left(x_1 + \frac{1}{2}\right)\right) \cdot \sin^2\left(\pi\left(x_2 + \frac{1}{2}\right)\right)$$

and with periodic boundary conditions, so that $u_0(\mathbf{x}) \equiv u(t=0,\mathbf{x}) \equiv u(t=1,\mathbf{x})$.

The numerical experiments are performed on a sequence of unstructured quasi-uniform triangular meshes of decreasing average meshsizes $h = 2^{-\ell}$, for $\ell = 3, 4, 5, 6, 7$. The resulting approximation errors E_p in the L^p-norms, $p \in \{1, 2, \infty\}$, together with the corresponding convergence rates k_p, for kernels $\phi_{2,2}$ and $\phi_{2,3}$, respectively, are recorded in Tables 6.1 and 6.2.

Note that in the case of thin-plate spline WENO reconstruction, we obtain second order convergence (see Table 6.1), whereas for WENO reconstruction by the kernel

TABLE 6.1
Linear advection. WENO reconstruction by $\phi_{2,2}$ on quasi-uniform meshes.

h	$E_1(h)$	k_1	$E_2(h)$	k_2	$E_\infty(h)$	k_∞
1/8	$5.3421 \cdot 10^{-2}$	–	$6.9206 \cdot 10^{-2}$	–	$1.9900 \cdot 10^{-1}$	–
1/16	$9.9088 \cdot 10^{-3}$	2.44	$1.3099 \cdot 10^{-2}$	2.40	$4.2914 \cdot 10^{-2}$	2.21
1/32	$2.1862 \cdot 10^{-3}$	2.17	$3.0085 \cdot 10^{-3}$	2.12	$1.1495 \cdot 10^{-2}$	1.90
1/64	$5.3530 \cdot 10^{-4}$	2.03	$7.3156 \cdot 10^{-4}$	2.04	$3.1629 \cdot 10^{-3}$	1.86
1/128	$1.2837 \cdot 10^{-4}$	2.06	$1.7544 \cdot 10^{-4}$	2.07	$8.3581 \cdot 10^{-4}$	1.92

TABLE 6.2
Linear advection. WENO reconstruction by $\phi_{2,3}$ on quasi-uniform meshes.

h	$E_1(h)$	k_1	$E_2(h)$	k_2	$E_\infty(h)$	k_∞
1/8	$6.1728 \cdot 10^{-2}$	–	$7.3862 \cdot 10^{-2}$	–	$1.8427 \cdot 10^{-1}$	–
1/16	$7.6627 \cdot 10^{-3}$	3.01	$9.3616 \cdot 10^{-3}$	2.98	$2.5205 \cdot 10^{-2}$	2.87
1/32	$1.0337 \cdot 10^{-3}$	2.89	$1.2984 \cdot 10^{-3}$	2.85	$3.5693 \cdot 10^{-2}$	2.82
1/64	$1.3658 \cdot 10^{-4}$	2.92	$1.6920 \cdot 10^{-4}$	2.94	$5.1608 \cdot 10^{-4}$	2.80
1/128	$1.7192 \cdot 10^{-5}$	2.99	$2.2355 \cdot 10^{-5}$	2.92	$7.0106 \cdot 10^{-5}$	2.88

$\phi_{2,3}$ in (3.4) we obtain third order convergence (see Table 6.2). These convergence rates comply with the theoretical results in [11] concerning local approximation orders for Lagrange interpolation by polyharmonic splines. We remark that the numerical results presented here are quite comparable with those in [14] (where polynomial WENO reconstruction is used), both in terms of accuracy and of convergence rates. The overall computational cost, however, when using polyharmonic spline reconstructions is smaller than that in the case of polynomial reconstruction, due to a smaller number of total stencils used (cf. the discussion in Section 4.2).

6.2. Burgers' Equation. We consider solving the nonlinear inviscid Burgers' equation

$$u_t + \frac{1}{2}\left(u^2\right)_{x_1} + \frac{1}{2}\left(u^2\right)_{x_2} = 0 \qquad \text{where } \mathbf{x} = (x_1, x_2) \tag{6.1}$$

for $u \equiv u(t, \mathbf{x}) : [0, 0.1] \times [-1, 1]^2 \to \mathbb{R}$, with initial condition

$$u_0(\mathbf{x}) \equiv u(0, \mathbf{x}) = \frac{1}{4} + \frac{1}{2}\sin(\pi(x_1 + x_2))$$

along with periodic boundary conditions. The exact solution u of this problem is given by the solution of the implicit equation

$$u = \frac{1}{4} + \frac{1}{2}\sin(\pi((x_1 - ut) + (x_2 - ut))).$$

The numerical experiments are performed on a sequence of unstructured quasi-uniform triangular meshes of decreasing average meshsizes $h = 2^{-\ell}$, for $\ell = 3, 4, 5, 6, 7$. The numerical results are shown in Tables 6.3 and 6.4. Note that the obtained convergence rates are similar to those in the previous numerical example concerning linear advection and, in particular, comply also with the theoretical results in [11]. Finally, the numerical results presented here are comparable with those in [14] (for polynomial WENO reconstruction), but at smaller computational costs, due to a smaller number of stencils.

TABLE 6.3
Burgers' equation. WENO reconstruction by $\phi_{2,2}$ on quasi-uniform meshes.

h	$E_1(h)$	k_1	$E_2(h)$	k_2	$E_\infty(h)$	k_∞
1/8	$8.1771 \cdot 10^{-2}$	–	$6.2890 \cdot 10^{-2}$	–	$1.8409 \cdot 10^{-1}$	–
1/16	$1.8045 \cdot 10^{-2}$	2.18	$1.4170 \cdot 10^{-2}$	2.15	$4.3240 \cdot 10^{-2}$	2.09
1/32	$4.4844 \cdot 10^{-3}$	2.00	$3.4782 \cdot 10^{-3}$	1.92	$1.2590 \cdot 10^{-2}$	1.78
1/64	$1.0862 \cdot 10^{-3}$	2.04	$1.1468 \cdot 10^{-3}$	1.78	$3.4926 \cdot 10^{-3}$	1.85
1/128	$2.6412 \cdot 10^{-4}$	2.04	$2.8472 \cdot 10^{-4}$	2.01	$9.4887 \cdot 10^{-4}$	1.88

TABLE 6.4
Burgers' equation. WENO reconstruction by $\phi_{2,3}$ on quasi-uniform meshes.

h	$E_1(h)$	k_1	$E_2(h)$	k_2	$E_\infty(h)$	k_∞
1/8	$6.3527 \cdot 10^{-2}$	–	$4.8526 \cdot 10^{-2}$	–	$1.5243 \cdot 10^{-1}$	–
1/16	$9.9128 \cdot 10^{-3}$	2.68	$7.3650 \cdot 10^{-3}$	2.72	$2.4624 \cdot 10^{-2}$	2.63
1/32	$1.3373 \cdot 10^{-3}$	2.89	$1.0215 \cdot 10^{-3}$	2.85	$3.4390 \cdot 10^{-3}$	2.84
1/64	$1.8292 \cdot 10^{-4}$	2.87	$1.3497 \cdot 10^{-4}$	2.92	$4.6394 \cdot 10^{-4}$	2.89
1/128	$2.3672 \cdot 10^{-5}$	2.95	$1.7106 \cdot 10^{-5}$	2.98	$8.6155 \cdot 10^{-5}$	2.81

6.3. The Smolarkiewicz Deformational Flow Test. We apply the proposed ADER method to the Smolarkiewicz deformational flow test [26], being regarded as a challenging benchmark problem for the evaluation of numerical methods for atmospheric flow problems. In this case, we consider solving the hyperbolic equation

$$u_t + \sigma_1(\mathbf{x})u_{x_1} + \sigma_2(\mathbf{x})u_{x_2} = 0 \qquad \text{where } \mathbf{x} = (x_1, x_2)$$

on the computational domain $\Omega = [100, 100]^2$, where

$$\sigma_1(\mathbf{x}) = 8k \sin(kx_1)\sin(kx_2) \quad \text{and} \quad \sigma_2(\mathbf{x}) = 8k \cos(kx_1)\cos(kx_2)$$

for $k = 4\pi/100$. The highly deformational velocity field produces symmetric counter-rotating vortices (displayed in Figure 6.1), resulting in a multiscale behaviour of the flow. The initial condition is given by

$$u_0(\mathbf{x}) = \begin{cases} 1 - r(\mathbf{x})/15 & \text{for } r(\mathbf{x}) \leq 15; \\ 0 & \text{otherwise;} \end{cases}$$

where $r(\mathbf{x}) = \sqrt{(x_1 - 50)^2 + (x_2 - 50)^2}$, i.e., the compactly supported surface $u_0(\mathbf{x})$ is given by a cone of unit height and radius 15 centred at the midpoint $(50, 50)$ of Ω. Figure 6.1 shows the steady velocity field, along with a contour plot for the cone $u_0(\mathbf{x})$. Note that the support of the initial condition $u_0(\mathbf{x})$ overlaps with six vortices.

The analytical solution $u(t, \mathbf{x})$ of the Smolarkiewicz deformational flow test exhibits spiral distributions of mass densities winding gradually tighter (at increasing time) within the square vortex cells (we refer to [28] for a detailed discussion on the Smolarkiewicz deformational flow test). Therefore, as the solution $u(t, \mathbf{x})$ evolves in time, this results in fine filaments of the solution's profile, thereby introducing smaller scales, which may become very small relative to the resolution of the triangular mesh.

In the application of the proposed ADER method to the Smolarkiewicz deformational flow test, we work with thin-plate spline WENO reconstruction on an unstructured quasi-uniform triangular mesh of average meshsize $h = 1$ and for a constant

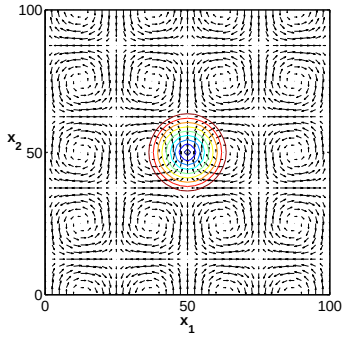

FIG. 6.1. *Smolarkiewicz deformational flow test. Velocity field and contours of initial condition.*

time step size $\tau^n \equiv \tau = T/10000$, where $T = 2637.6$, following [26]. Figure 6.2 shows our numerical solution at times $t = 3T/200$, $3T/100$, $9T/200$, $3T/50$, $4T/50$, and $T/10$, respectively.

Also, cross-sections of the numerical solution along the horizontal straight line $\{(x_1, 50) : 0 \leq x_1 \leq 100\} \subset \Omega$ are, along with the corresponding cross-sections of the exact solution $u(t, \mathbf{x})$, provided in Figure 6.3 at times $t = T/100$, $3T/200$, $3T/50$, and $T/10$, respectively.

We found that the numerical solution approximates the analytical solution well in the time interval $[0, T/50]$ (e.g. for times $t_1 = T/100$ and $t_2 = 3T/200$), even in the vicinity of sharp gradients. However, for larger times t (e.g. for times $t_3 = 3T/50$ and $t_4 = T/10$) the approximation deteriorates and a reasonable amount of numerical diffusion is observed.

The deterioration of accuracy of the numerical solution can be explained by the increasingly multiscale behaviour of the exact solution as time evolves. Indeed, the smallest scales of the exact solution are, at any time $t \in [0, T/50]$, well-resolved by the meshsize of the (fixed) triangular mesh used. For larger times, however, the numerical solution fails to capture the increasingly finer scales as the mesh is kept fixed. Nevertheless, the numerical stability of the proposed method is evident at both the scale resolving and the non-resolving regimes.

7. Numerical Results on Adaptive Triangular Meshes. In this section, we develop an adaptive version of the proposed ADER method. This requires customised rules for the adaptive refinement and coarsening of the triangular mesh. The adaption rules, developed in Section 7.2, rely on a suitable local error indicator, described in Section 7.1. We prefer to keep the discussion in Sections 7.1 and 7.2 rather short, as the construction of the adaption rules relies on a basic concept presented in the previous work [14], where further details concerning the utilised mesh adaptation strategy can be found.

7.1. The Error Indicator. The utilised error indicator is based on local polyharmonic spline interpolation from discrete cell averages. This makes sense insofar as the local error indicator essentially needs to measure the approximation quality of the numerical solution (computed through the utilised kernel-based WENO reconstruction) locally around a cell T.

The error indicator for a cell T is reconstructed from cell averages of cells lying

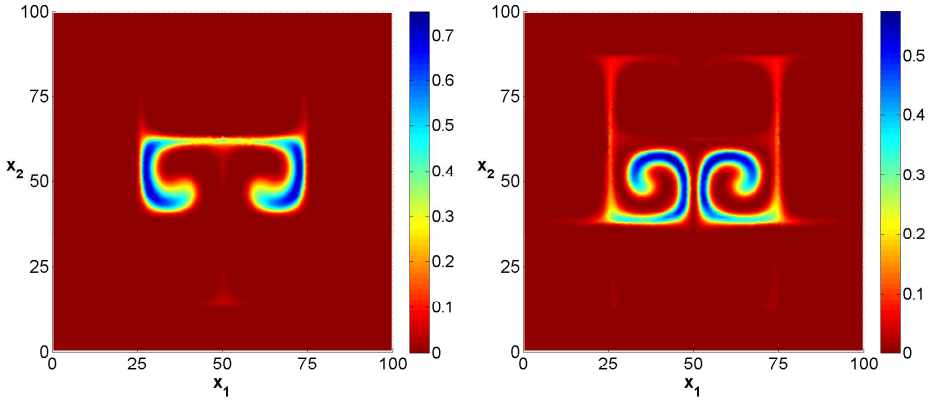

(a) $t = 3T/200$

(b) $t = 3T/100$

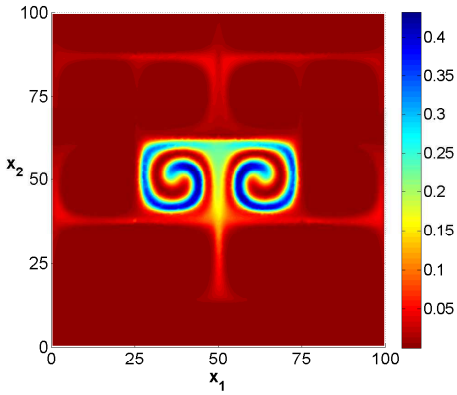

(c) $t = 9T/200$

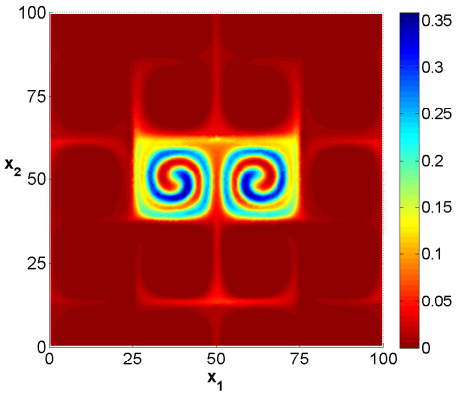

(d) $t = 3T/50$

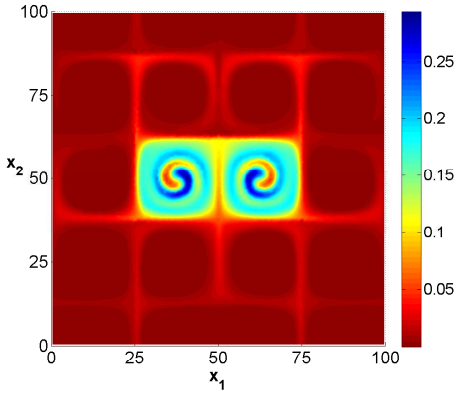

(e) $t = 4T/50$

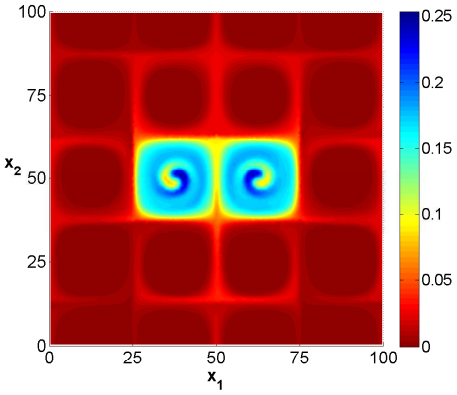

(f) $t = T/10$

FIG. 6.2. *Smolarkiewicz's deformational flow test. Numerical solution at six different times.*

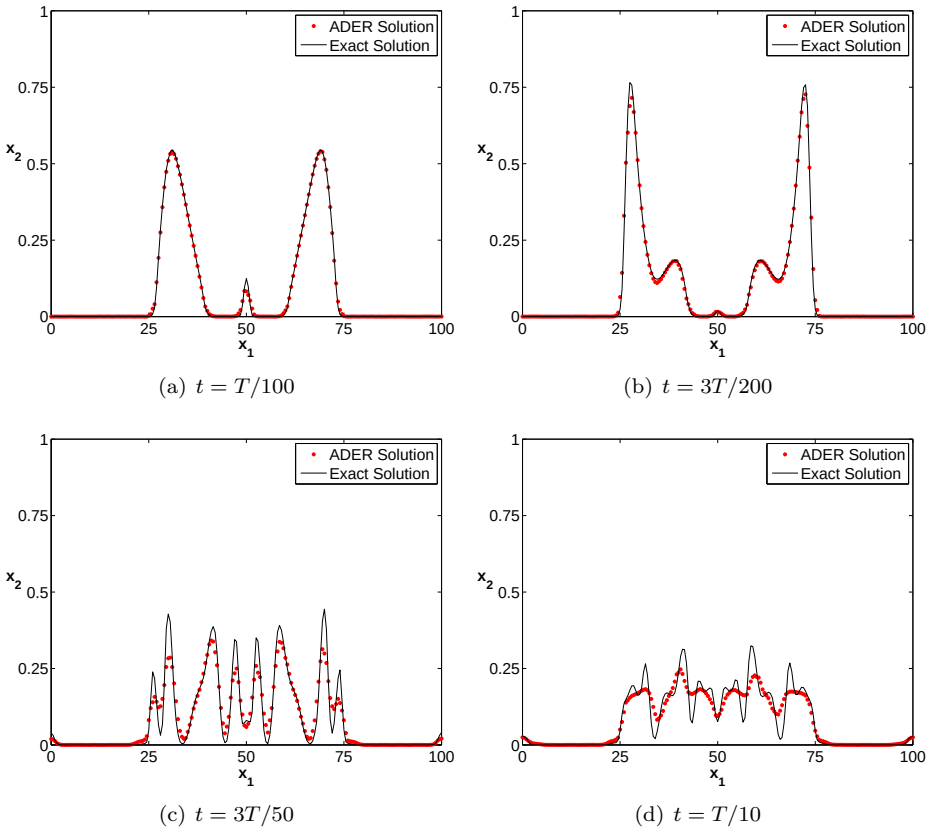

(a) $t = T/100$ (b) $t = 3T/200$

(c) $t = 3T/50$ (d) $t = T/10$

FIG. 6.3. *Smolarkiewicz's deformational flow test. Solution profiles along the line* $x_2 \equiv 50$.

in the *Moore neighbourhood* of T. Recall that the Moore neighbourhood

$$\mathcal{N}_{\mathrm{M}}(T) := \{R \in \mathcal{T} \setminus \{T\} : R \cap T \neq \emptyset\} \subset \mathcal{T}$$

of a cell $T \in \mathcal{T}$ contains all cells in (the conforming shape-regular triangulation) $\mathcal{T}$ which are sharing a common face or a common vertex with T. Note that the Moore neighbourhood $\mathcal{N}_{\mathrm{M}}(T)$ of T does *not* contain T.

To each cell $T \in \mathcal{T}$, we assign its cell average value $\bar{u}_T$ to the barycentre $\mathbf{b}_T$ of T, i.e., $\bar{u}_T \equiv \bar{u}(\mathbf{b}_T)$, and we compute the (unique) polyharmonic spline interpolant s_T satisfying the Lagrangian interpolation conditions

$$s_T(\mathbf{b}_R) = \bar{u}(\mathbf{b}_R) \qquad \text{for all } R \in \mathcal{N}_{\mathrm{M}}(T).$$

The local error indicator $\varepsilon : \mathcal{T} \mapsto [0, \infty)$ is then defined by

$$\varepsilon_T := |\bar{u}(\mathbf{b}_T) - s_T(\mathbf{b}_T)| \qquad \text{for } T \in \mathcal{T}. \tag{7.1}$$

Note that the error indicator ε_T estimates, for any $T \in \mathcal{T}$, the local approximation behaviour in the neighbourhood of the cell $T \in \mathcal{T}$: a large value of ε_T indicates a large approximation error around T, while a small value of ε_T indicates otherwise. As supported by the numerical examples in the following Sections 7.3 and 7.4, the error indicator serves to detect discontinuities and sharp gradients of the solution u.

7.2. Mesh Adaptation. The local error indicator (7.1) provides a useful criterion reflecting which regions of the computational mesh require higher resolution and which regions are well approximated. When higher resolution is indicated, the mesh is locally refined, whereas in regions where the solution appears to be well approximated, the mesh is locally coarsened, so as to equidistribute the error over the computational mesh.

The following mesh adaptation strategy is used to mark individual cells T in $\mathcal{T}$ for refinement or coarsening. To this end, let $\vartheta_{\mathrm{r}}, \vartheta_{\mathrm{d}}$ be two (user-defined) threshold values, satisfying $0 < \vartheta_{\mathrm{d}} \leq \vartheta_{\mathrm{r}} < 1$, and let $\varepsilon^* := \max_{T\in\mathcal{T}} \varepsilon_T$. A cell $T \in \mathcal{T}$ is chosen for refinement, if $\varepsilon_T > \vartheta_{\mathrm{r}} \cdot \varepsilon^*$, whereas T is chosen for coarsening, if $\varepsilon_T < \vartheta_{\mathrm{d}} \cdot \varepsilon^*$. Note that this splits the current cells of $\mathcal{T}$ into three classes – to be refined, to be coarsened, or neither/nor to be refined/coarsened. In the numerical experiments of the following two Subsections 7.3-7.4, we choose the values $\vartheta_{\mathrm{r}} = 0.05$ and $\vartheta_{\mathrm{d}} = 0.01$.

Following along the lines of [14], the refinement/coarsening of individual cells is accomplished as follows. A triangular cell $T \in \mathcal{T}(t^n)$ is, at time step n, refined by the insertion of its barycenter $\mathbf{b}_T$ as a new node of the triangulation. A triangular cell $T \in \mathcal{T}(t^n)$ is coarsened by removing its three nodes from the triangulation. At each time step, after all the new nodes have been inserted and the nodes of the triangles to be coarsened have been removed, the triangulation is then updated by a local Delaunay re-triangulation, giving $\mathcal{T}(t^{n+1})$. We remark that the local re-triangulation is a computationally inexpensive.

Particular care has to be taken when transferring the cell average data from $\mathcal{T}(t^n)$ onto a modified $\mathcal{T}(t^{n+1})$ in order to maintain numerical conservation and to ensure (as much as possible) that this process does not generate oscillations near discontinuities. To this end, a strategy similar to the one presented in [12] is used, which we briefly describe here for completeness. First, the intersection area (known also as a *tile*) of a triangle $T \in \mathcal{T}(t^{n+1})$ with the triangles that it overlaps in $\mathcal{T}(t^n)$ is computed using the *chasing algorithm* of O'Rourke [19].

Once the area of intersection tiles is computed, we compute the mass contained in the tiles. Suppose $T \in \mathcal{T}(t^{n+1})$ overlaps with ℓ cells $T_i \in \mathcal{T}(t^n)$, $i = 1, \ldots, \ell$, so that $T = \cup_{i=1}^{\ell}(T \cap T_i)$. Then, the total mass of $T \in \mathcal{T}(t^{n+1})$ is given by

$$m_T := \sum_{i=1}^{\ell} m_{T\cap T_i} \qquad \text{with } m_{T\cap T_i} := \int_{T\cap T_i} u_h(t^n, \mathbf{x})\, d\mathbf{x}, \qquad i = 1, \ldots, \ell, \tag{7.2}$$

where u_h is the restriction of the WENO interpolant on $T_i \in \mathcal{T}(t^n)$ over $T \cap T_i$. The cell average of $T \in \mathcal{T}(t^{n+1})$ is then defined by

$$\bar{u}_T = \frac{1}{|T|} m_T \qquad \text{for all} \quad T \in \mathcal{T}(t^{n+1}).$$

Once the cell averages for all $T \in \mathcal{T}(t^{n+1})$ have been computed, the WENO reconstruction is then performed on triangulation $\mathcal{T}(t^{n+1})$.

7.3. Burgers' Equation Revisited. We consider solving Burgers' equation (6.1) again on $\Omega = [-0.5, 0.5]^2$, with the initial condition

$$u_0(\mathbf{x}) = \begin{cases} \exp\left(\frac{\|\mathbf{x}-\mathbf{c}\|^2}{\|\mathbf{x}-\mathbf{c}\|^2 - R^2}\right) & \text{for } \|\mathbf{x}-\mathbf{c}\| < R; \\ 0 & \text{otherwise;} \end{cases} \tag{7.3}$$

where $R = 0.15$ and $\mathbf{c} = (-0.2, -0.2)^{\mathrm{T}}$.

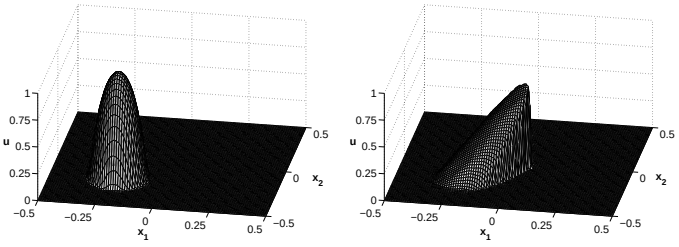

(a) $t = 0$ (b) $t = 0.4$

(c) $t = 0.8$ (d) $t = 1.2$

FIG. 7.1. *Burgers' equation. Numerical solution at four different times.*

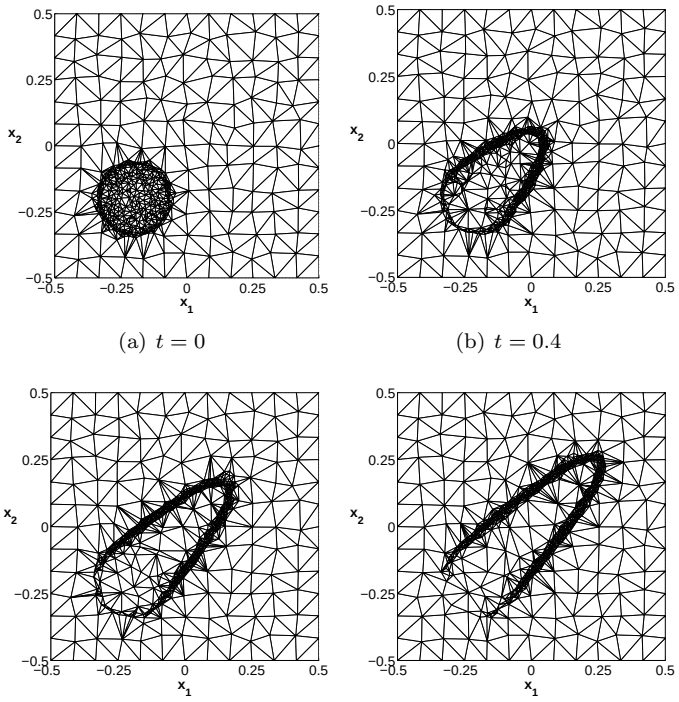

(a) $t = 0$ (b) $t = 0.4$

(c) $t = 0.8$ (d) $t = 1.2$

FIG. 7.2. *Burgers' equation. Adaptive meshes at four different times.*

Recall that even for smooth initial data, such as in (7.3), the solution of Burgers' equation may spontaneously develop discontinuities, corresponding to shocks. This behaviour leads to computational challenges which (among others) motivates the development of *adaptive* numerical methods, in order to balance the required accuracy versus the computational complexity. We apply the adaptive version of the proposed ADER method described above, using the thin-plate spline kernel $\phi_{2,2}$ in the WENO reconstruction step.

The numerical simulation is initialised on mesh $\mathcal{T}^0$ (shown in Figure 7.2(a)), which is well-adapted to the initial condition u_0 using 5 iterations of the adaptive algorithm. The mesh is subject to further adaptive modifications during the simulation, using one iteration of the adaptive algorithm per time-step, as described above. The resulting numerical solution is shown in Figure 7.1 at four different times $t = 0$, $t = 0.4$, $t = 0.8$, and $t = 1.2$. The corresponding adaptive meshes are shown in Figure 7.2.

Note that the adaptive triangular mesh captures the shape of the solution u very well. In particular, the propagation of the shock front is well-resolved during the simulation, see Figures 7.1 and 7.2. Indeed, in regions, where the solution u is rather smooth, the triangular mesh is rather coarse. This helps reduce the required computational costs, while maintaining the method's accuracy. In comparison with the numerical results in [14] (where polynomial WENO reconstruction is used), we observe comparable shock front resolution (and thus comparable accuracy), but at a significantly smaller number of triangular cells (cf. Figures 6 and 7 in [14]). We attribute this to the customized construction of the WENO weights, being defined by using the native space (Beppo-Levi) semi-norm (3.5) of the kernel-based interpolation.

7.4. Two-Phase Flow in Porous Media – The Five-Spot Problem. Finally, we turn to another challenging benchmark problem concerning two-phase flow simulation in petroleum reservoirs. This particular application scenario is concerning the displacement of one fluid, say oil, by another, say water, within a petroleum reservoir. A somewhat simplified, but fairly realistic model problem for petroleum reservoir simulation is the *Buckley-Leverett model* [3], concerning two-phase flow of two immiscible and incompressible fluids, say water and oil, within a homogeneous porous medium, where diffusive effects, such as capillary pressure, are ignored and gravitational forces are neglected.

The resulting *Buckley-Leverett equation* is a time-dependent hyperbolic equation,

$$\frac{\partial u}{\partial t} + \mathbf{v} \cdot \nabla F(u) = 0 \qquad \text{where} \quad F(u) = \frac{u^2}{u^2 + \sigma(1-u)^2}, \tag{7.4}$$

where $\mathbf{v}$ is the *velocity field* and σ is the ratio of the two fluids' viscosities. The value of the solution $u \equiv u(t, \mathbf{x})$ is the saturation of the wetting fluid (water) in the non-wetting fluid (oil).

Here, we consider solving the Buckley-Leverett equation for the test case scenario of the popular *five-spot problem*. In this test case, the pores over the square-shaped oil reservoir $\Omega = [-0.5, 0.5]^2$ are assumed to be filled with the non-wetting fluid (oil, $u \equiv 0$) at initial time $t = 0$, before the wetting fluid (water, $u \equiv 1$) is injected through a single injection well, located at the centre $\mathbf{o} := (0, 0)$ of the computational domain Ω.

As the simulation advances in time, the oil is displaced by the water towards the four corner points $\mathcal{C} := \{(\pm 0.5, \pm 0.5)\}$ of Ω. The water injection is modelled by the initial condition

$$u_0(\mathbf{x}) = \begin{cases} 1 & \text{for } \|\mathbf{x}\| < 0.02; \\ 0 & \text{otherwise.} \end{cases} \tag{7.5}$$

Moreover, we use a steady velocity field $\mathbf{v} = -\nabla \mathbf{p}$, where the pressure is given by

$$\mathbf{p}(\mathbf{x}) \equiv \mathbf{p}(t, \mathbf{x}) = \sum_{\mathbf{c} \in \mathcal{C}} \log(\|\mathbf{x} - \mathbf{c}\|) - \log(\|\mathbf{x} - \mathbf{o}\|) \quad \text{for all } \mathbf{x} \in \Omega, t \in I.$$

In the application of petroleum reservoir simulation, the location of the shock front at the interface of the two fluids, water and oil, is of particular importance [13].

We apply the proposed adaptive ADER method to numerically solve the initial value problem (7.4),(7.5) of the five-spot problem, using thin-plate spline WENO reconstruction.

Our numerical results are reflected by Figures 8.1 and 8.2. Figure 8.2 displays a sequence of adaptive triangular meshes generated by the proposed ADER method at six different times, $t = 0$, $t = 0.013840$, $t = 0.033595$, $t = 0.050461$, $t = 0.068518$, and $t = 0.084685$. The corresponding numerical solution u is shown in Figure 8.1, where the progress of the oil displacement by water is visualised through the evolution of the time-dependent saturation $u \equiv u(t, \mathbf{x})$ of water in oil.

Note that the shock front propagation is captured quite effectively by the adaptive triangular mesh (see Figure 8.2). Moreover, in regions of the solution's rarefraction wave the triangular mesh is re-coarsened after the shock front passed through them. This leads to significant savings in computational costs, while maintaining the method's accuracy. The well-adapted distribution of triangles supports the utility of the proposed adaption rules.

8. Conclusions. We have proposed an adaptive ADER finite volume method for the numerical solution of scalar hyperbolic conservations laws. The ADER method, relying on unstructured simplicial meshes, combines high order flux evaluations with high order WENO reconstruction using polyharmonic spline kernels. This leads to a finite volume method of arbitrary high order.

Polyharmonic spline WENO reconstruction schemes are very flexible, due the variable dimension of their corresponding ansatz spaces. This extra flexibility allows us to work with WENO stencils of variable sizes, unlike in previous polynomial reconstructions, thereby leading to significant savings in computational costs. Moreover, WENO reconstruction by polyharmonic splines is numerically stable. The stable implementation of polyharmonic spline WENO reconstruction relies on a customised preconditioner, which is developed in this paper. Finally, polyharmonic spline reconstruction leads to a natural choice for an oscillation indicator (as required in the WENO reconstruction scheme), given by the energy functional of their associated Sobolev (Beppo-Levi) space.

We have combined the polyharmonic spline WENO reconstruction scheme with a previous mesh adaptation strategy relying on an a posteriori error indicator. This results in an efficient mesh modification scheme, which achieves to capture singularities of the solution, such as sharp gradients and shock fronts, quite effectively.

The good performance of the resulting adaptive ADER method is demonstrated by several challenging test case scenarios, including Burgers' equation, the Smolarkiewicz's deformational flow test, and the five-spot problem.

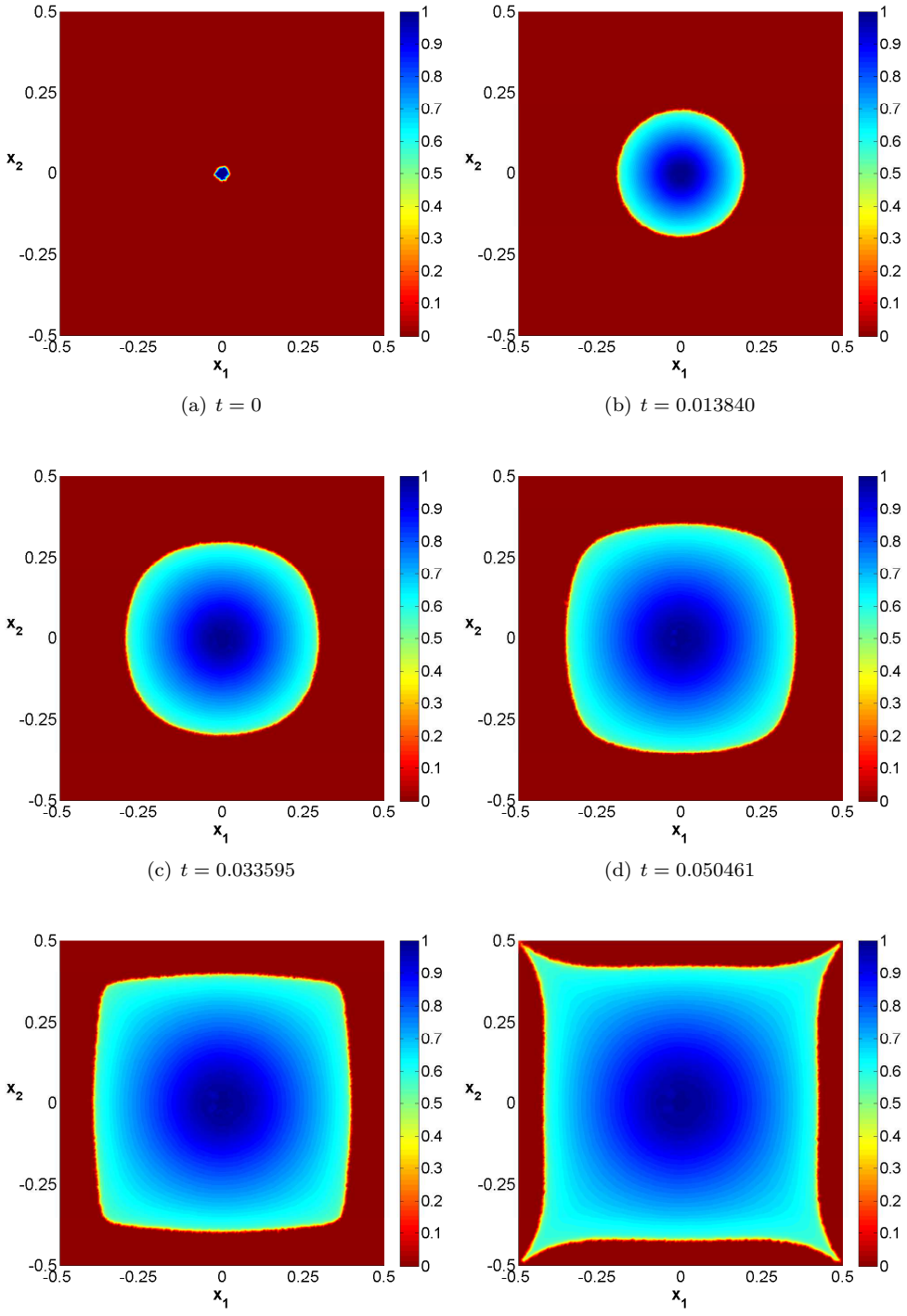

(a) $t = 0$ (b) $t = 0.013840$

(c) $t = 0.033595$ (d) $t = 0.050461$

(e) $t = 0.068518$ (f) $t = 0.084685$

FIG. 8.1. *The five spot problem. Solution u (saturation of water in oil) at six different times.*

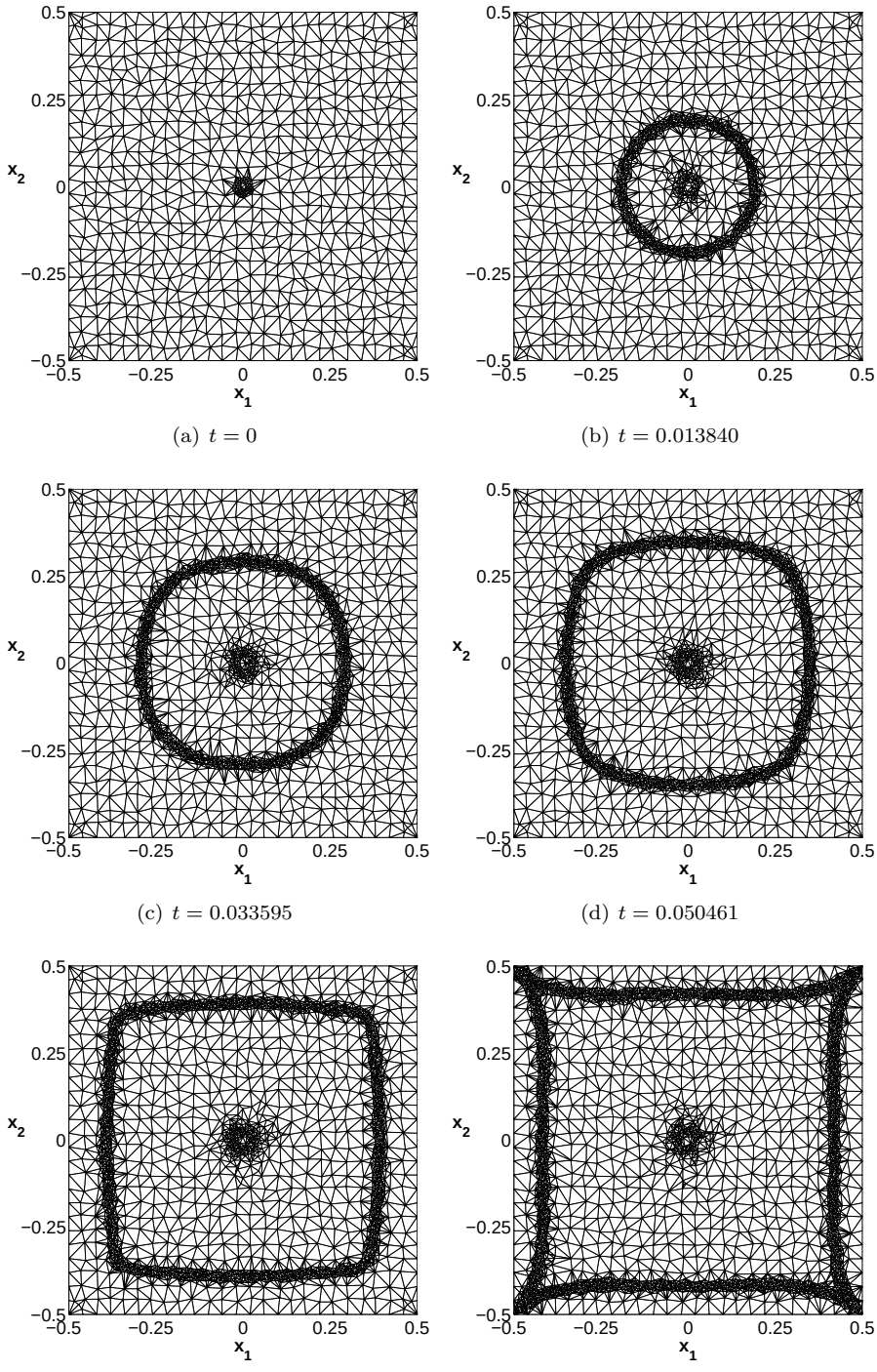

(a) $t = 0$ (b) $t = 0.013840$

(c) $t = 0.033595$ (d) $t = 0.050461$

(e) $t = 0.068518$ (f) $t = 0.084685$

FIG. 8.2. *The five spot problem. Adaptive triangular mesh at six different times.*

Acknowledgments. The first author acknowledges the support of The Commonwealth Scholarship Commission in the UK. The third author is supported by the priority program DFG-SPP 1324 of the Deutsche Forschungsgemeinschaft (DFG).

REFERENCES

[1] R. Abgrall, *On essentially non-oscillatory schemes on unstructured meshes: analysis and implementation*, J. Comput. Phys., 114 (1994), pp. 45–58.
[2] T. Aboiyar, *Non-oscillatory finite volume methods for conservation laws on unstructured grids*, PhD thesis, University of Leicester, 2008.
[3] M. D. Buckley and M. C. Leverett, *Mechanisms of fluid displacements in sands*, Trans. AIME, 146 (1942), pp. 107–116.
[4] J. Duchon, *Interpolation des fonctions de deux variables suivant le principe de la flexion des plaques minces*, RAIRO Analyse Numerique, 10 (1976), pp. 5–12.
[5] M. Dumbser and M. Käser, *Arbitrary high order non-oscillatory finite volume schemes on unstructured meshes for linear hyperbolic systems*, Journal of Computational Physics, 221 (2007), pp. 693–723.
[6] M. Dumbser and C.-D. Munz, *ADER discontinuous Galerkin schemes for aeroacoustics*, Comptes Rendus Mécanique, (2004).
[7] ———, *Arbitrary high order discontinuous Galerkin schemes*, in Numerical methods for hyperbolic and kinetic problems, vol. 7 of IRMA Lect. Math. Theor. Phys., Eur. Math. Soc., Zürich, 2005, pp. 295–333.
[8] O. Friedrich, *Weighted essentially non-oscillatory schemes for the interpolation of mean values on unstructured grids*, J. Comput. Phys., 144 (1998), pp. 194–212.
[9] S. Gottlieb and C.-W. Shu, *Total variation diminishing Runge-Kutta schemes*, Math. Comp., 67 (1998), pp. 73–85.
[10] C. Hu and C.-W. Shu, *Weighted essentially non-oscillatory schemes on triangular meshes*, J. Comput. Phys., 150 (1999), pp. 97–127.
[11] A. Iske, *On the approximation order and numerical stability of local Lagrange interpolation by polyharmonic splines*, in Modern Developments in Multivariate Approximation, vol. 145 of Internat. Ser. Numer. Math., Birkhäuser, Basel, 2003, pp. 153–165.
[12] ———, *On the construction of mass conservative and meshless adaptive particle advection methods*, in Advances in Meshfree Techniques, V. Leitao, C. Alves, and C. Duarte, eds., Springer, Dordrecht, 2007, pp. 169–186.
[13] K. H. Karlsen, K.-A. Lie, and N. H. Risebro, *A fast marching method for reservoir simulation*, Comput. Geosci., 4 (2000), pp. 185–206.
[14] M. Käser and A. Iske, *ADER schemes on adaptive triangular meshes for scalar conservation laws*, J. Comput. Phys., 205 (2005), pp. 486–508.
[15] R. J. LeVeque, *Finite volume methods for hyperbolic problems*, Cambridge Texts in Applied Mathematics, Cambridge University Press, Cambridge, 2002.
[16] C. A. Micchelli, *Interpolation of scattered data: distance matrices and conditionally positive definite functions*, Constr. Approx., 2 (1986), pp. 11–22.
[17] K. W. Morton and T. Sonar, *Finite volume methods for hyperbolic conservation laws*, Acta Numerica, 16 (2007), pp. 155–238.
[18] F. J. Narcowich and J. D. Ward, *Norm estimates for the inverses of a general class of scattered-data radial-function interpolation matrices*, J. Approx. Theory, 69 (1992), pp. 84–109.
[19] J. O'Rourke, *Computational geometry in C*, Cambridge University Press, Cambridge, 1994.
[20] S. J. Ruuth and R. J. Spiteri, *Two barriers on strong-stability-preserving time discretization methods*, J. Sci. Comput., 17 (2002), pp. 211–220.
[21] T. Schwartzkopff, M. Dumbser, and C.-D. Munz, *Fast high order ADER schemes for linear hyperbolic equations and their numerical dissipation and dispersion*, J. Comput. Phys., 197 (2004), pp. 532–539.
[22] T. Schwartzkopff, C.-D. Munz, and E. F. Toro, *ADER: a high-order approach for linear hyperbolic systems*, J. Sci. Comput., 17 (2002), pp. 231–240.
[23] T. Schwartzkopff, C.-D. Munz, E. F. Toro, and R. C. Millington, *The ADER approach in 2d*, in Discrete Modelling and Discrete Algorithms on Continuum Mechanics, T. Sonar and I. Thomas, eds., Berlin, 2001, Logos, pp. 207–216.
[24] C.-W. Shu, *High order ENO and WENO schemes for computational fluid dynamics*, in High-order methods for computational physics, vol. 9 of Lect. Notes Comput. Sci. Eng., Springer, Berlin, 1999, pp. 439–582.

[25] C.-W. Shu, *High order weighted essentially nonoscillatory schemes for convection dominated problems*, SIAM Review, 51 (2009), pp. 82–126.
[26] P. Smolarkiewicz, *The multi-dimensional Crowley advection scheme*, Mon. Wea. Rev., 110 (1982), pp. 1968–1983.
[27] T. Sonar, *On the construction of essentially non-oscillatory finite volume approximations to hyperbolic conservation laws on general triangulations: polynomial recovery, accuracy and stencil selection*, Comput. Methods Appl. Mech. Engrg., 140 (1997), pp. 157–181.
[28] A. Staniforth, J. Cote, and J. Pudykiewicsz, Comments on *"Smolarkiewicz's deformational flow"*, Mon. Wea. Rev., 115 (1987), pp. 894–900.
[29] V. A. Titarev and E. F. Toro, *ADER: arbitrary high order Godunov approach*, J. Sci. Comput., 17 (2002), pp. 609–618.
[30] ———, *Finite-volume WENO schemes for three-dimensional conservation laws*, J. Comput. Phys., 201 (2004), pp. 238–260.
[31] ———, *ADER schemes for three-dimensional non-linear hyperbolic systems*, J. Comput. Phys., 204 (2005), pp. 715–736.
[32] E. F. Toro and A. Hidalgo, *ADER finite volume schemes for diffusion-reaction equations*, Appl. Numer. Math., 59 (2009), pp. 73–100.
[33] E. F. Toro and R. C. Millington, *The ADER approach to linear advection.*, in ECCOMAS Computational Fluid Dynamics Conference, 2001.
[34] E. F. Toro, R. C. Millington, and L. A. M. Nejad, *Towards very high order Godunov schemes*, in Godunov methods (Oxford, 1999), Kluwer/Plenum, New York, 2001, pp. 907–940.
[35] E. F. Toro and V. A. Titarev, *Solution of the generalized Riemann problem for advection-reaction equations*, R. Soc. Lond. Proc. Ser. A Math. Phys. Eng. Sci., 458 (2002), pp. 271–281.
[36] ———, *ADER schemes for scalar non-linear hyperbolic conservation laws with source terms in three-space dimensions*, J. Comput. Phys., 202 (2005), pp. 196–215.
[37] ———, *Derivative Riemann solvers for systems of conservation laws and ADER methods*, J. Comput. Phys., 212 (2006), pp. 150–165.
[38] W. R. Wolf and J. L. F. Azevedo, *High-order ENO and WENO schemes for unstructured grids*, Internat. J. Numer. Methods Fluids, 55 (2007), pp. 917–943.

Preprint Series DFG-SPP 1324

http://www.dfg-spp1324.de

Reports

[1] R. Ramlau, G. Teschke, and M. Zhariy. A Compressive Landweber Iteration for Solving Ill-Posed Inverse Problems. Preprint 1, DFG-SPP 1324, September 2008.

[2] G. Plonka. The Easy Path Wavelet Transform: A New Adaptive Wavelet Transform for Sparse Representation of Two-dimensional Data. Preprint 2, DFG-SPP 1324, September 2008.

[3] E. Novak and H. Woźniakowski. Optimal Order of Convergence and (In-) Tractability of Multivariate Approximation of Smooth Functions. Preprint 3, DFG-SPP 1324, October 2008.

[4] M. Espig, L. Grasedyck, and W. Hackbusch. Black Box Low Tensor Rank Approximation Using Fibre-Crosses. Preprint 4, DFG-SPP 1324, October 2008.

[5] T. Bonesky, S. Dahlke, P. Maass, and T. Raasch. Adaptive Wavelet Methods and Sparsity Reconstruction for Inverse Heat Conduction Problems. Preprint 5, DFG-SPP 1324, January 2009.

[6] E. Novak and H. Woźniakowski. Approximation of Infinitely Differentiable Multivariate Functions Is Intractable. Preprint 6, DFG-SPP 1324, January 2009.

[7] J. Ma and G. Plonka. A Review of Curvelets and Recent Applications. Preprint 7, DFG-SPP 1324, February 2009.

[8] L. Denis, D. A. Lorenz, and D. Trede. Greedy Solution of Ill-Posed Problems: Error Bounds and Exact Inversion. Preprint 8, DFG-SPP 1324, April 2009.

[9] U. Friedrich. A Two Parameter Generalization of Lions' Nonoverlapping Domain Decomposition Method for Linear Elliptic PDEs. Preprint 9, DFG-SPP 1324, April 2009.

[10] K. Bredies and D. A. Lorenz. Minimization of Non-smooth, Non-convex Functionals by Iterative Thresholding. Preprint 10, DFG-SPP 1324, April 2009.

[11] K. Bredies and D. A. Lorenz. Regularization with Non-convex Separable Constraints. Preprint 11, DFG-SPP 1324, April 2009.

[12] M. Döhler, S. Kunis, and D. Potts. Nonequispaced Hyperbolic Cross Fast Fourier Transform. Preprint 12, DFG-SPP 1324, April 2009.

[13] C. Bender. Dual Pricing of Multi-Exercise Options under Volume Constraints. Preprint 13, DFG-SPP 1324, April 2009.

[14] T. Müller-Gronbach and K. Ritter. Variable Subspace Sampling and Multi-level Algorithms. Preprint 14, DFG-SPP 1324, May 2009.

[15] G. Plonka, S. Tenorth, and A. Iske. Optimally Sparse Image Representation by the Easy Path Wavelet Transform. Preprint 15, DFG-SPP 1324, May 2009.

[16] S. Dahlke, E. Novak, and W. Sickel. Optimal Approximation of Elliptic Problems by Linear and Nonlinear Mappings IV: Errors in L_2 and Other Norms. Preprint 16, DFG-SPP 1324, June 2009.

[17] B. Jin, T. Khan, P. Maass, and M. Pidcock. Function Spaces and Optimal Currents in Impedance Tomography. Preprint 17, DFG-SPP 1324, June 2009.

[18] G. Plonka and J. Ma. Curvelet-Wavelet Regularized Split Bregman Iteration for Compressed Sensing. Preprint 18, DFG-SPP 1324, June 2009.

[19] G. Teschke and C. Borries. Accelerated Projected Steepest Descent Method for Nonlinear Inverse Problems with Sparsity Constraints. Preprint 19, DFG-SPP 1324, July 2009.

[20] L. Grasedyck. Hierarchical Singular Value Decomposition of Tensors. Preprint 20, DFG-SPP 1324, July 2009.

[21] D. Rudolf. Error Bounds for Computing the Expectation by Markov Chain Monte Carlo. Preprint 21, DFG-SPP 1324, July 2009.

[22] M. Hansen and W. Sickel. Best m-term Approximation and Lizorkin-Triebel Spaces. Preprint 22, DFG-SPP 1324, August 2009.

[23] F.J. Hickernell, T. Müller-Gronbach, B. Niu, and K. Ritter. Multi-level Monte Carlo Algorithms for Infinite-dimensional Integration on $\mathbb{R}^{\mathbb{N}}$. Preprint 23, DFG-SPP 1324, August 2009.

[24] S. Dereich and F. Heidenreich. A Multilevel Monte Carlo Algorithm for Lévy Driven Stochastic Differential Equations. Preprint 24, DFG-SPP 1324, August 2009.

[25] S. Dahlke, M. Fornasier, and T. Raasch. Multilevel Preconditioning for Adaptive Sparse Optimization. Preprint 25, DFG-SPP 1324, August 2009.

[26] S. Dereich. Multilevel Monte Carlo Algorithms for Lévy-driven SDEs with Gaussian Correction. Preprint 26, DFG-SPP 1324, August 2009.

[27] G. Plonka, S. Tenorth, and D. Roşca. A New Hybrid Method for Image Approximation using the Easy Path Wavelet Transform. Preprint 27, DFG-SPP 1324, October 2009.

[28] O. Koch and C. Lubich. Dynamical Low-rank Approximation of Tensors. Preprint 28, DFG-SPP 1324, November 2009.

[29] E. Faou, V. Gradinaru, and C. Lubich. Computing Semi-classical Quantum Dynamics with Hagedorn Wavepackets. Preprint 29, DFG-SPP 1324, November 2009.

[30] D. Conte and C. Lubich. An Error Analysis of the Multi-configuration Time-dependent Hartree Method of Quantum Dynamics. Preprint 30, DFG-SPP 1324, November 2009.

[31] C. E. Powell and E. Ullmann. Preconditioning Stochastic Galerkin Saddle Point Problems. Preprint 31, DFG-SPP 1324, November 2009.

[32] O. G. Ernst and E. Ullmann. Stochastic Galerkin Matrices. Preprint 32, DFG-SPP 1324, November 2009.

[33] F. Lindner and R. L. Schilling. Weak Order for the Discretization of the Stochastic Heat Equation Driven by Impulsive Noise. Preprint 33, DFG-SPP 1324, November 2009.

[34] L. Kämmerer and S. Kunis. On the Stability of the Hyperbolic Cross Discrete Fourier Transform. Preprint 34, DFG-SPP 1324, December 2009.

[35] P. Cerejeiras, M. Ferreira, U. Kähler, and G. Teschke. Inversion of the noisy Radon transform on $SO(3)$ by Gabor frames and sparse recovery principles. Preprint 35, DFG-SPP 1324, January 2010.

[36] T. Jahnke and T. Udrescu. Solving Chemical Master Equations by Adaptive Wavelet Compression. Preprint 36, DFG-SPP 1324, January 2010.

[37] P. Kittipoom, G. Kutyniok, and W.-Q Lim. Irregular Shearlet Frames: Geometry and Approximation Properties. Preprint 37, DFG-SPP 1324, February 2010.

[38] G. Kutyniok and W.-Q Lim. Compactly Supported Shearlets are Optimally Sparse. Preprint 38, DFG-SPP 1324, February 2010.

[39] M. Hansen and W. Sickel. Best m-Term Approximation and Tensor Products of Sobolev and Besov Spaces – the Case of Non-compact Embeddings. Preprint 39, DFG-SPP 1324, March 2010.

[40] B. Niu, F.J. Hickernell, T. Müller-Gronbach, and K. Ritter. Deterministic Multi-level Algorithms for Infinite-dimensional Integration on $\mathbb{R}^{\mathbb{N}}$. Preprint 40, DFG-SPP 1324, March 2010.

[41] P. Kittipoom, G. Kutyniok, and W.-Q Lim. Construction of Compactly Supported Shearlet Frames. Preprint 41, DFG-SPP 1324, March 2010.

[42] C. Bender and J. Steiner. Error Criteria for Numerical Solutions of Backward SDEs. Preprint 42, DFG-SPP 1324, April 2010.

[43] L. Grasedyck. Polynomial Approximation in Hierarchical Tucker Format by Vector-Tensorization. Preprint 43, DFG-SPP 1324, April 2010.

[44] M. Hansen und W. Sickel. Best m-Term Approximation and Sobolev-Besov Spaces of Dominating Mixed Smoothness - the Case of Compact Embeddings. Preprint 44, DFG-SPP 1324, April 2010.

[45] P. Binev, W. Dahmen, and P. Lamby. Fast High-Dimensional Approximation with Sparse Occupancy Trees. Preprint 45, DFG-SPP 1324, May 2010.

[46] J. Ballani and L. Grasedyck. A Projection Method to Solve Linear Systems in Tensor Format. Preprint 46, DFG-SPP 1324, May 2010.

[47] P. Binev, A. Cohen, W. Dahmen, R. DeVore, G. Petrova, and P. Wojtaszczyk. Convergence Rates for Greedy Algorithms in Reduced Basis Methods. Preprint 47, DFG-SPP 1324, May 2010.

[48] S. Kestler and K. Urban. Adaptive Wavelet Methods on Unbounded Domains. Preprint 48, DFG-SPP 1324, June 2010.

[49] H. Yserentant. The Mixed Regularity of Electronic Wave Functions Multiplied by Explicit Correlation Factors. Preprint 49, DFG-SPP 1324, June 2010.

[50] H. Yserentant. On the Complexity of the Electronic Schrödinger Equation. Preprint 50, DFG-SPP 1324, June 2010.

[51] M. Guillemard and A. Iske. Curvature Analysis of Frequency Modulated Manifolds in Dimensionality Reduction. Preprint 51, DFG-SPP 1324, June 2010.

[52] E. Herrholz and G. Teschke. Compressive Sensing Principles and Iterative Sparse Recovery for Inverse and Ill-Posed Problems. Preprint 52, DFG-SPP 1324, July 2010.

[53] L. Kämmerer, S. Kunis, and D. Potts. Interpolation Lattices for Hyperbolic Cross Trigonometric Polynomials. Preprint 53, DFG-SPP 1324, July 2010.

[54] G. Kutyniok and W.-Q Lim. Shearlets on Bounded Domains. Preprint 54, DFG-SPP 1324, July 2010.

[55] A. Zeiser. Wavelet Approximation in Weighted Sobolev Spaces of Mixed Order with Applications to the Electronic Schrödinger Equation. Preprint 55, DFG-SPP 1324, July 2010.

[56] G. Kutyniok, J. Lemvig, and W.-Q Lim. Compactly Supported Shearlets. Preprint 56, DFG-SPP 1324, July 2010.

[57] A. Zeiser. On the Optimality of the Inexact Inverse Iteration Coupled with Adaptive Finite Element Methods. Preprint 57, DFG-SPP 1324, July 2010.

[58] S. Jokar. Sparse Recovery and Kronecker Products. Preprint 58, DFG-SPP 1324, August 2010.

[59] T. Aboiyar, E. H. Georgoulis, and A. Iske. Adaptive ADER Methods Using Kernel-Based Polyharmonic Spline WENO Reconstruction. Preprint 59, DFG-SPP 1324, August 2010.